

# Stabilized finite element formulations for liquid membranes and their application to droplet contact

Roger A. Sauer <sup>1</sup>

*Aachen Institute for Advanced Study in Computational Engineering Science (AICES), RWTH Aachen University, Templergraben 55, 52056 Aachen, Germany*

Published<sup>2</sup> in *Int. J. Numer. Meth. Fluids*, DOI: [10.1002/fld.3905](https://doi.org/10.1002/fld.3905)

Submitted on 4. October 2013, Accepted on 24. February 2014

---

## Abstract

A liquid membrane formulation is presented that is suitable to analyze liquid films and their contact behavior. The governing strong form and weak form equations are presented in the general framework of the curvilinear coordinate system that is used for the surface description of the membrane. Particular emphasis is placed on the stabilization of the in-plane equilibrium equations, which is essential for the quasi-static description of liquid membranes. Two new stabilization schemes are proposed that affect only the in-plane membrane behavior while leaving the out-of-plane membrane behavior unaffected. Further emphasis is placed on the description of line contact needed to impose non-trivial contact angles. The proposed formulation is discretized within the finite element method considering both standard Lagrange-based and isogeometric NURBS-based finite elements. Computational contact algorithms are formulated both for surface and line contact. The complete linearization of the discretized formulation is given. A large range of numerical examples is presented in order to illustrate the different physical aspects that are captured by the proposed formulation. The examples are further used to analyze the performance of the new stabilization schemes.

**Keywords:** computational contact mechanics, curvilinear coordinates, isogeometric analysis, nonlinear finite element methods, rough surface contact, wetting.

---

## 1 Introduction

This work is concerned with a general computational formulation for liquid membranes. Liquid membranes, which characterize the free surface behavior of liquids, are especially important at small length scales where surface effects can become dominating. Some cases are always governed by membrane behavior, irrespective of scale. Examples are droplets, bubbles and liquid coats. The mechanics of liquid membranes is governed by the surface tension of liquids, which is typically considered as a constant isotropic stress state. The consequence of this is the quasi-static instability of the in-plane membrane behavior. This instability needs to be addressed in computations. In a more general context, e.g. in the case of solid membranes, the membrane is characterized by more general stress states. However, instabilities also exist for solid membranes, most prominently the wrinkling instability. The membrane description considered here is equally applicable for solid and liquid membranes, such that transitions can be described. The focus, though, is placed on liquid membranes, proposing efficient schemes for

---

<sup>1</sup>corresponding author, email: [sauer@aices.rwth-aachen.de](mailto:sauer@aices.rwth-aachen.de)

<sup>2</sup>This pdf is a personal version of an article whose final publication is available at [www.onlinelibrary.wiley.com](http://www.onlinelibrary.wiley.com)

their stabilization in computations and discussing their application to contact problems. One aspect of membrane contact is the occurrence of distinct angles at contact boundaries, which is also addressed here. The numerical discretization is treated here in the framework of the finite element method.

There is a range of earlier work on computational formulations for liquid membranes and their contact behavior. The first finite element approach is the model by Brown et al. [1]. Their formulation only considers the out-of-plane membrane behavior. This circumvents the instability but severely restricts the range of deformation. More general are the approaches by Brakke [2] and Iliev [3]. These are based on energy minimization but are not in the framework of a Galerkin-type FE formulation, as is considered here. Such a formulation has also been considered by Ma and Klug [4] for the description of lipid bilayers. There, the authors propose an in-plane stabilization based on the previous iterate, which can be viewed as algorithmic viscosity. For dynamic problems, the physical viscosity and the inertia of the membrane and an enclosed fluid will stabilize the system. Dynamic problems have been studied by Arroyo and DeSimone [5] and Rahimi and Arroyo [6], where an axisymmetric FE implementation based on B-splines is presented. Also the aspect of contact has been considered in earlier work: Sprittles and Shikhmurzaev [7] present a FE method to describe wetting considering the bulk CFD problem with free surface boundary conditions. In order to impose contact angles both natural and essential boundary conditions are considered. The authors note that only the latter gives satisfactory results. Radcliffe et al. [8] simulate the steady-state contact between droplets and rigid obstacles based on an artificial dynamical relaxation technique that is non-FEM. In the above formulations, contact is described by boundary conditions along the contact line. In this case the contact surface does not need to be discretized. An alternative approach, considered here, is to model the contact surface and consider a computational contact algorithm as is used for solids [9; 10]. Such an approach has been proposed by Sauer et al. [11] both for solid and liquid membranes. This formulation has several advantages over the conventional approaches as is listed below. It is finally noted that we are interested here in an explicit surface description, i.e. a description where the surface is discretized directly, based on surface finite elements. There is a wide range of other approaches, indirect surface descriptions based on the bulk discretization or non-FE approaches. Examples are embedded surface methods [12], level set methods [13], particle methods [14], volume of fluid methods [15], spectral boundary elements [16; 17], molecular dynamics [18], Lattice-Boltzmann approaches [19], and density functional theory [20].

Within this work several new aspects are introduced to the computational modeling of liquid membranes: Two new stabilization schemes for liquid membranes are developed, a contact formulation is used to describe surface contact, and, at the contact line, a new contact angle formulation for rough substrate surfaces is developed. The new formulation is based on the weak form of the membrane equations including the contributions for surface and line contact and using suitable contact algorithms for both. The weak form is discretized within a Galerkin based finite element method providing the full tangent matrix that is needed for implicit computations. The formulation readily admits  $C^1$ -smooth NURBS elements, which are also considered here. A broad range of examples is presented in order to illustrate the range of applications and study the accuracy of the proposed stabilization schemes for various element classes. Not discussed here are contact angle hysteresis and sliding contact. Also, we restrict ourselves to quasi-static conditions where there is no fluid flow, neither internally nor within the membrane surface. These are left for future work.

There are several advantages of the proposed contact surface description:

- one can straightforwardly apply classical contact algorithms for the description of surface contact of liquids,

- the setup is indispensable for the detection of new and lost contact,
- the setup is indispensable for contact between deforming bodies (liquid–solid or liquid–liquid),
- the contact line does not need to be modeled explicitly for contact angles  $\theta_c = \pi$  since this it is determined automatically by the contact algorithm, and
- it is useful to study the dynamics of decreasing contact angles, starting from  $\theta_c = \pi$ .

The proposed contact description leads to a closure of the droplet surface with has several advantageous of its own:

- it is very helpful for the evaluation of surface integrals, e.g. to determine the enclosed volume,
- it is required for modeling non-constant surface tension within the solid–liquid interface
- it thus allows the consideration of more general constitutive models for liquid membranes, and
- it is useful as a boundary for flow computations of the enclosed media.

The remainder of this paper is organized as follows. Sec. 2 presents the governing strong and weak equations for the stabilization of quasi-static liquid membranes considering surface and line contact. The corresponding finite element formulation is then discussed in Sec. 3. A second stabilization approach, applied at the discretized level, is also presented in Sec. 3. Sec. 4 then presents several numerical examples that illustrate the performance of the proposed formulation for various loading and contact cases. Finally, conclusions are drawn in Sec. 5.

## 2 Governing equations

This section describes the theoretical framework of the proposed liquid membrane formulation. The problem setup is introduced, and its kinematics, constitution, surface equilibrium, stabilization, line equilibrium, and strong and weak form equations are presented. The description relies on differential geometry. For an overview of the basic relations of differential geometry, we refer to earlier work [11].

### 2.1 Problem setup

We begin with discussing the general 3D setup that is considered here for liquid membranes as they for example appear in bubbles and droplets, see Fig. 1. Here,  $\mathcal{S}$  denotes the set of all surface points of the liquid membrane. It contains the two subdomains  $\mathcal{S}_{\text{SL}}$  and  $\mathcal{S}_{\text{LG}}$ , marking the solid-liquid and liquid-gas interfaces, such that

$$\mathcal{S} = \mathcal{S}_{\text{SL}} \cup \mathcal{S}_{\text{LG}} , \quad \mathcal{S}_{\text{SL}} \cap \mathcal{S}_{\text{LG}} = \mathcal{C} . \quad (1)$$

Here,  $\mathcal{C}$  denotes the contact line on  $\mathcal{S}$  that forms the interface between  $\mathcal{S}_{\text{SL}}$  and  $\mathcal{S}_{\text{LG}}$ . Further,  $\partial\mathcal{B}$  denotes the set of all surface points of the body  $\mathcal{B}$ , which, here, is considered as a rigid

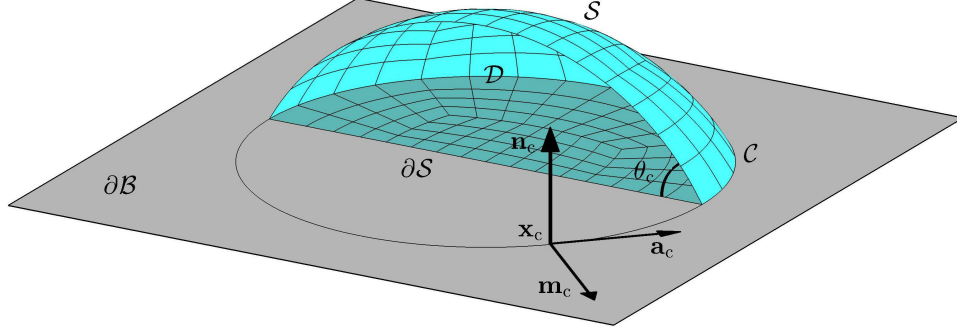


Figure 1: Problem setup: A liquid membrane in contact with a rigid solid.

half-space. The upper surface contains the two subdomains  $\partial\mathcal{B}_{\text{SL}}$  and  $\partial\mathcal{B}_{\text{SG}}$  that mark the solid-liquid and solid-gas interfaces on  $\partial\mathcal{B}$  such that

$$\partial\mathcal{B} = \partial\mathcal{B}_{\text{SL}} \cup \partial\mathcal{B}_{\text{SG}} , \quad \partial\mathcal{B}_{\text{SL}} \cap \partial\mathcal{B}_{\text{SG}} = \mathcal{C}_{\mathcal{B}} . \quad (2)$$

In theory,  $\partial\mathcal{B}_{\text{SL}} = \mathcal{S}_{\text{SL}}$  and  $\mathcal{C}_{\mathcal{B}} = \mathcal{C}$ , but computationally differences may appear, e.g. due to a penalty regularization of contact. The boundary of surface  $\mathcal{S}$  is decomposed into displacement and traction prescribed domains, such that

$$\partial\mathcal{S} = \partial_u\mathcal{S} \cup \partial_t\mathcal{S} . \quad (3)$$

Here we also require that  $\partial_u\mathcal{S} \cap \partial_t\mathcal{S} = \emptyset$ , unless the prescribed displacements and tractions are perpendicular to each other. On each subdomain, statement (3) extends to

$$\partial\mathcal{S}_I = \partial_u\mathcal{S}_I \cup \partial_t\mathcal{S}_I \cup \mathcal{C} , \quad I = \text{SL or LG} , \quad (4)$$

and we further have

$$\partial_u\mathcal{S} = \partial_u\mathcal{S}_{\text{SL}} \cup \partial_u\mathcal{S}_{\text{LG}} , \quad \partial_t\mathcal{S} = \partial_t\mathcal{S}_{\text{SL}} \cup \partial_t\mathcal{S}_{\text{LG}} . \quad (5)$$

Points on  $\mathcal{S}$  are described by the bases  $\{\mathbf{a}_1, \mathbf{a}_2, \mathbf{n}\}$  and  $\{\mathbf{a}^1, \mathbf{a}^2, \mathbf{n}\}$ , where  $\mathbf{n}$  is the outward surface normal, and  $\mathbf{a}_\alpha$  and  $\mathbf{a}^\alpha$  are the covariant and contra-variant tangent vectors of  $\mathcal{S}$ .<sup>3</sup> They are constructed from the parameterization of  $\mathcal{S}$  [11]. Points on  $\mathcal{C}$  are described by the basis  $\{\mathbf{m}_c, \mathbf{a}_c, \mathbf{n}_c\}$ , where  $\mathbf{m}_c$  is tangent to  $\partial\mathcal{B}$  and normal to  $\partial\mathcal{S}_{\text{SL}}$ ,  $\mathbf{a}_c$  is the tangent vector of  $\mathcal{C}$ , and  $\mathbf{n}_c$  is the normal of  $\partial\mathcal{B}_c$ . In theory this basis is orthogonal, but computationally this may not be satisfied exactly as is shown later.

Large deformations are considered here such that we need to distinguish the deformed configuration of the membrane structure from its undeformed reference configuration. Index ‘0’ is used to distinguish the reference sets from the current sets. Capital letters are used to distinguish reference vectors from current vectors. The displacement between the two membrane configurations is denoted as

$$\mathbf{u} = \mathbf{X} - \mathbf{x} , \quad \mathbf{X} \in \mathcal{S}_0 , \quad \mathbf{x} \in \mathcal{S} . \quad (6)$$

For further details of the kinematical description we refer to [11].

<sup>3</sup>Here and in the following all Greek indices run from 1 to 2, and imply summation when repeated.

## 2.2 Liquid membrane constitution

According to membrane assumption, we only consider in-plane stress components such that the stress tensor can be written as<sup>4</sup>

$$\boldsymbol{\sigma} = \sigma_{\alpha\beta} \mathbf{a}^\alpha \otimes \mathbf{a}^\beta = \sigma_\beta^\alpha \mathbf{a}_\alpha \otimes \mathbf{a}^\beta = \sigma^{\alpha\beta} \mathbf{a}_\alpha \otimes \mathbf{a}_\beta . \quad (7)$$

For liquid membranes, under quasi-static conditions, the surface stress state is hydrostatic, i.e.

$$\boldsymbol{\sigma} = \gamma \mathbf{1} , \quad (8)$$

with  $\mathbf{1} = \mathbf{a}_\alpha \otimes \mathbf{a}^\alpha = \mathbf{a}^\alpha \otimes \mathbf{a}_\alpha$ . The constant  $\gamma$  is the surface tension of the interface. For a liquid in contact,  $\gamma$  changes between  $\mathcal{S}_{\text{LG}}$  and  $\mathcal{S}_{\text{SL}}$ , assuming the values  $\gamma_{\text{LG}}$  to  $\gamma_{\text{SL}}$ . From (7) and (8) follows,

$$\sigma_{\alpha\beta} = \gamma a_{\alpha\beta} , \quad \sigma_\beta^\alpha = \gamma \delta_\beta^\alpha , \quad \sigma^{\alpha\beta} = \gamma a^{\alpha\beta} , \quad (9)$$

where  $a_{\alpha\beta} = \mathbf{a}_\alpha \cdot \mathbf{a}_\beta$ ,  $\delta_\beta^\alpha = \mathbf{a}^\alpha \cdot \mathbf{a}_\beta$  and  $a^{\alpha\beta} = \mathbf{a}^\alpha \cdot \mathbf{a}^\beta$  are various components of the metric tensor. This stress state looks very simple, but it leads to a major difficulty in computations: The formulation is unstable, since the stress is independent of the deformation. At the interface  $\partial\mathcal{B}_{\text{SG}}$ , we also have an interface stress  $\boldsymbol{\sigma}$ . This is also considered in form (7), where  $\gamma$  is now equal to  $\gamma_{\text{SG}}$ , which is the isotropic surface tension of interface  $\partial\mathcal{B}_{\text{SG}}$ . According to Cauchy's formula, the membrane traction<sup>5</sup> on the surface  $\perp \mathbf{a}^\alpha$  is given by

$$\mathbf{t}^\alpha = \boldsymbol{\sigma} \mathbf{a}^\alpha . \quad (10)$$

According to (8), we have  $\mathbf{t}^\alpha = \gamma \mathbf{a}^\alpha$ .

## 2.3 Equilibrium of liquid membranes

Membrane equilibrium is governed by the field equation [21]

$$\mathbf{t}_{;\alpha}^\alpha + \mathbf{f} = \mathbf{0} \quad \text{on } \mathcal{S} . \quad (11)$$

For liquids,  $\mathbf{t}^\alpha$  is given by the relations of Sec. 2.2, but also other constitutive models can be considered in this context. For conservative systems, (11) can be derived from a potential [22].  $\mathbf{f}$  denotes the body force acting on  $\mathcal{S}$ . Here we consider the contributions

$$\mathbf{f} = \mathbf{f}_f + \mathbf{f}_c + \bar{\mathbf{f}} \quad (12)$$

representing fluid forces, contact forces and external forces. The body force can be decomposed as

$$\mathbf{f} = f^\alpha \mathbf{a}_\alpha + p \mathbf{n} , \quad (13)$$

where  $f^\alpha := f_f^\alpha + f_c^\alpha + \bar{f}^\alpha$  is the (contra-variant) in-plane component of  $\mathbf{f}$  and  $p := p_f - p_c - \bar{p}$  is the out-of-plane component of  $\mathbf{f}$ .<sup>6</sup> With this, field equation (11) can be decomposed into [11]

$$\begin{aligned} \sigma^{\alpha\beta}_{;\beta} + f^\alpha &= 0 \quad (\text{in-plane equilibrium}), \\ \sigma^{\alpha\beta} b_{\alpha\beta} + p &= 0 \quad (\text{out-of-plane equilibrium}). \end{aligned} \quad (14)$$

<sup>4</sup>Due to the symmetry of the stress tensor  $\sigma_\beta^\alpha = \sigma_\beta^\alpha = \sigma_\beta^\alpha$

<sup>5</sup>Note that, in general,  $\mathbf{t}^\alpha$  is not the physical traction on the surface  $\perp \mathbf{a}^\alpha$ , as  $\mathbf{a}^\alpha$  is not normalized.

<sup>6</sup>The minus signs on  $p_c$  and  $\bar{p}$  are introduced so that  $p_c$  and  $\bar{p}$  correspond to positive pressures acting on the outside surface of the droplet.

For liquids, we have

$$\sigma^{\alpha\beta}_{;\beta} = \gamma(\mathbf{a}^{\alpha}_{;\beta} \cdot \mathbf{a}^{\beta} + \mathbf{a}^{\alpha} \cdot \mathbf{a}^{\beta}_{;\beta}) \quad (15)$$

according to (9). Since  $\mathbf{a}^{\alpha}_{;\beta}$  and  $\mathbf{a}^{\gamma}$  are perpendicular, this implies that  $\sigma^{\alpha\beta}_{;\beta} = 0$ . Consequently,  $f^{\alpha} = 0$ . Thus, if there are no external forces present,

$$f^{\alpha}_{\text{f}} + f^{\alpha}_{\text{c}} = 0, \quad (16)$$

i.e. the tangential contact forces equilibrate the tangential fluid forces. For quasi-static conditions  $f^{\alpha}_{\text{f}}$  and thus  $f^{\alpha}_{\text{c}}$  are zero. Eq. (14.1) is therefore identically satisfied for hydro-static conditions – regardless of the deformation. This physical instability carries over to the computational description and it therefore needs to be addressed, as is done by the two stabilization schemes presented in Secs. 2.4 and 3.5. For liquids, the out-of-plane equation (14.2) yields

$$2H\gamma + p = 0, \quad 2H := b^{\alpha}_{\alpha}, \quad (17)$$

which is the well known Young-Laplace equation. If the contact surface is flat, i.e.  $b^{\alpha}_{\alpha} = 0$ , we find (for  $\bar{p} = 0$ )

$$p_{\text{c}} = p_{\text{f}}, \quad (18)$$

i.e. the contact pressure is equal to the inside fluid pressure. This is not true for curved contact surfaces. For incompressible fluids, the fluid pressure  $p_{\text{f}}$  is associated with the incompressibility constraint. For quasi-static conditions,  $p_{\text{f}}$  can be written as

$$p_{\text{f}} = p_{\text{v}} + p_{\text{h}}, \quad (19)$$

where

$$p_{\text{h}} = \rho \mathbf{g} \cdot \mathbf{x} \quad (20)$$

is the (known) hydrostatic pressure and  $p_{\text{v}}$  is the capillary pressure that remains associated with the constraint. Here  $\rho$  is the density of the pressure causing medium, and  $\mathbf{g}$  is the gravity vector. The value of  $p_{\text{v}}$  is then the (constant) datum pressure at the origin.

On the boundary, the usual Dirichlet and Neumann boundary conditions

$$\begin{aligned} \mathbf{u} &= \bar{\mathbf{u}} \quad \text{on } \partial_u \mathcal{S}, \\ \mathbf{t} &= \bar{\mathbf{t}} \quad \text{on } \partial_t \mathcal{S}, \end{aligned} \quad (21)$$

are considered. The traction on boundary  $\partial_t \mathcal{S}$ , according to Cauchy's formula, is given by

$$\mathbf{t} = \boldsymbol{\sigma} \mathbf{m}, \quad (22)$$

where  $\mathbf{m} = m_{\alpha} \mathbf{a}^{\alpha}$  is the outward unit normal of  $\partial_t \mathcal{S}$ . From (10) follows that  $\mathbf{t} = m_{\alpha} \mathbf{t}^{\alpha}$ . For liquids

$$\mathbf{t} = \gamma \mathbf{m}. \quad (23)$$

On the free boundary  $\partial_t \mathcal{S}$ ,  $\bar{\mathbf{t}}$  is only supported if it is parallel to the deformed membrane plane.

It is noted that liquid droplets are closed membranes that have no boundary. For uniqueness and for symmetry reasons, it is however important to provide numerical boundary conditions. At symmetry boundaries (cf. Fig. 1) we have a zero in-plane Dirichlet BC perpendicular to the boundary and a zero in-plane Neumann BC tangential to the boundary.

## 2.4 Liquid membrane stabilization

Due to (15), the in-plane equilibrium equation is satisfied for any  $\gamma$ , regardless of the deformation of the membrane. The quasi-static description of liquid membranes is therefore unstable. This property leads to singular FE matrices. The FE formulation thus needs to be stabilized.

One approach is to solve the out-of-plane equation on a fixed mesh, like the spherical mesh used by Brown et al. [1] for droplets. However, this approach is problematic for large deformations: In some cases, the deformed droplet is not uniquely represented by the fixed mesh, so that the problem cannot be solved anymore by that approach. Therefore the mesh needs to be updated during deformation. Ideally this can be done by considering the in-plane equilibrium equation. Since this equation is initially unstable, a stabilization stress is introduced that is dependent on the in-plane deformation. To maintain the consistency with the out-of-plane membrane behavior, this stabilization stress is formulated such that it does not affect out-of-plane equilibrium.

In [11] a stabilization stress was proposed in the form

$$\sigma_{\text{sta}}^{\alpha\beta} = \mu/J(A^{\alpha\beta} - a^{\alpha\beta}/J^2) . \quad (24)$$

This expression follows from the incompressible Neo-Hookean material model. For simplicity, the variant

$$\sigma_{\text{sta}}^{\alpha\beta} = \mu/J(A^{\alpha\beta} - a^{\alpha\beta}) \quad (25)$$

is considered here. We denote this original formulation as stabilization scheme ‘A’. Parameter  $\mu$  is a stabilization parameter that needs to be chosen. It is shown in [11] and in Sec. 4.1 that the numerical error decreases with  $\mu$ . However, as  $\mu$  decreases the stabilizing effect also vanishes.

In this work, two new stabilization schemes are proposed, that are much more robust and accurate (and thus more efficient) than the two original schemes presented above. They also avoid choosing a stabilization parameter. The two new schemes are both based on the stabilization stress

$$\sigma_{\text{sta}}^{\alpha\beta} = \mu/J(a_{\text{pre}}^{\alpha\beta} - a^{\alpha\beta}) , \quad (26)$$

where  $a_{\text{pre}}^{\alpha\beta}$  is taken from the previous load increment during computation. We denote this new formulation as stabilization scheme ‘a’. It adds the same stiffness to the system as (25), so it essentially has the same stabilizing effect. But it is much more accurate, since it adds much less (unphysical) stress to the system. This is due to the fact that, usually, several load steps need to be taken, such that the difference  $a_{\text{pre}}^{\alpha\beta} - a^{\alpha\beta}$  tends to be small. Parameter  $\mu$  therefore does not need to be picked particularly low. We will simply consider  $\mu$  fixed at  $\mu = \gamma$ .

As already noted, the stabilization stress is only included in the in-plane equilibrium, such that the out-of-plane equilibrium equation, which is the only physically meaningful equation for quasi-static liquid membranes, is not affected. The field equations for the liquid membrane then read

$$\begin{aligned} (\gamma a^{\alpha\beta} + \sigma_{\text{sta}}^{\alpha\beta})_{;\beta} &= 0 \quad (\text{in-plane equilibrium}), \\ \gamma b_{\alpha}^{\alpha} + p &= 0 \quad (\text{out-of-plane equilibrium}). \end{aligned} \quad (27)$$

Here we have accounted for the fact that  $f^{\alpha} = 0$ , as shown in Sec. 2.3. For comparison, we will also examine the effect of applying  $\sigma_{\text{sta}}^{\alpha\beta}$  from (26) throughout, i.e. in both equations. This approach is denoted as stabilization scheme ‘a-t’. It is shown below that scheme ‘a-t’ is much less accurate than scheme ‘a’ (cf. Fig 6). Scheme ‘a-t’ is similar to the stabilization approach proposed in [4].

Further, a second, even more accurate stabilization scheme based on (26) and (27) can be constructed at the discretized level. This is presented in Sec. 3.5. This approach is denoted as stabilization scheme ‘P’. The numerical examples of Sec. 4 show that schemes ‘a’ and ‘P’ are very successfully in accurately describing the quasi-static behavior of liquid membranes.

## 2.5 Contact line equilibrium

We now discuss the force equilibrium at the contact line  $\mathcal{C}$ . Fig. 2 shows the line forces acting at  $\mathbf{x}_c \in \mathcal{C}$ . These are the tractions  $\mathbf{t}_{\text{SL}} = \gamma_{\text{SL}} \mathbf{m}_{\text{SL}} = \gamma_{\text{SL}} \mathbf{m}_c$ ,  $\mathbf{t}_{\text{LG}} = \gamma_{\text{LG}} \mathbf{m}_{\text{LG}}$  and  $\mathbf{t}_{\text{SG}} = \gamma_{\text{SG}} \mathbf{m}_{\text{SG}} =$

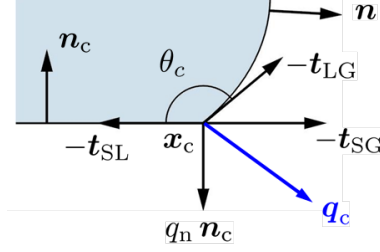


Figure 2: Equilibrium along the contact line  $\mathcal{C}$ .

$-\gamma_{\text{SG}} \mathbf{m}_c$  (due to (23)), and further, the traction  $\mathbf{q}_n = q_n \mathbf{n}_c$  that is needed to balance  $\mathbf{t}_{\text{LG}}$ . The equilibrium at the contact line can be written as

$$\mathbf{t}_{\text{SL}} + \mathbf{t}_{\text{LG}} = \mathbf{q}_c, \quad (28)$$

where we have introduced the traction

$$\mathbf{q}_c = \gamma_{\text{SG}} \mathbf{m}_c + q_n \mathbf{n}_c \quad (29)$$

shown in Fig. 2. The two components of  $\mathbf{q}_c$  are governed by the equations

$$\begin{aligned} \gamma_{\text{SG}} &= \gamma_{\text{SL}} + \gamma_{\text{LG}} \cos \theta_c, \\ q_n &= -\gamma_{\text{LG}} \sin \theta_c. \end{aligned} \quad (30)$$

Eq. (30.1) is also known as Young's equation.

## 2.6 Summary: Droplet strong form

Table 1 summarizes the main equations that govern liquid membranes in strong form. In this

1.	field equation, in general: $\mathbf{t}_{;\alpha}^\alpha + \mathbf{f} = \mathbf{0}$ on $\mathcal{S}$ for liquids the stabilized equations (27) are considered;
2.	membrane tractions: $\mathbf{t}^\alpha = \boldsymbol{\sigma} \mathbf{a}^\alpha$ , $\mathbf{t} = \boldsymbol{\sigma} \mathbf{m}$
3.	membrane stress: $\boldsymbol{\sigma} = \sigma^{\alpha\beta} \mathbf{a}_\alpha \otimes \mathbf{a}_\beta$ $\sigma^{\alpha\beta}$ is given by the relations of Secs. 2.2 and 2.4;
4.	contact surface constraint: $g_n = (\mathbf{x} - \mathbf{x}_p) \cdot \mathbf{n}_p \geq 0$ on $\mathcal{S}$
5.	volume constraint: $g_v = V_0 - V = 0$
6.	contact line equilibrium: $\mathbf{t}_{\text{SL}} + \mathbf{t}_{\text{LG}} = \mathbf{q}_c$ on $\mathcal{C}$
7.	boundary conditions: $\mathbf{u} = \bar{\mathbf{u}}$ on $\partial_u \mathcal{S}$ and $\mathbf{t} = \bar{\mathbf{t}}$ on $\partial_t \mathcal{S}$

Table 1: Summary of the strong form equations governing liquid membranes.

framework, two constraints are considered: The classical contact constraint [10]

$$g_n = (\mathbf{x} - \mathbf{x}_p) \cdot \mathbf{n}_p \geq 0 \quad \text{on } \mathcal{S}, \quad (31)$$

where  $\mathbf{n}_p$  denotes the surface normal of  $\partial\mathcal{B}$  at the closest projection point  $\mathbf{x}_p \in \partial\mathcal{B}$  of the membrane point  $\mathbf{x} \in \mathcal{S}$ , and the volume constraint

$$g_v = V_0 - V = 0, \quad (32)$$

where  $V$  and  $V_0$  denote the enclosed volumes of  $\mathcal{S}$  and  $\mathcal{S}_0$ .

The considered membrane model contains five physical model parameters. These are  $\gamma_{\text{LG}}$ ,  $\gamma_{\text{SL}}$ ,  $\gamma_{\text{SG}}$ ,  $V_0$  and  $\rho g$ . According to Eq. (30.1), one of the  $\gamma$ 's can be replaced by the contact angle.

## 2.7 Droplet weak form

The governing strong form equations are now transformed into weak form. Here, the constraints (31) and (32), as well as the Dirchlet BC and the constitutive relations of Secs. 2.2 and 2.4, are considered to remain enforced in strong form. The weak form is thus constructed from equilibria (11) and (28). Therefore, consider a virtual variation of the deformation,  $\mathbf{w}$ , that belongs to the set of all kinematically admissible deformations  $\mathcal{W}$  (i.e.  $\mathbf{w} = \mathbf{0}$  on  $\partial_u\mathcal{S}$ ). Following the standard approach, i.e. contracting (11), (21.2) and (28) by  $\mathbf{w}$ , integrating them over their respective domains, and summing the outcome, gives

$$\int_{\mathcal{S}} \mathbf{w} \cdot (\mathbf{t}_{;\alpha}^\alpha + \mathbf{f}) \, da + \int_{\partial_t\mathcal{S}} \mathbf{w} \cdot (\bar{\mathbf{t}} - \mathbf{t}) \, ds + \int_{\mathcal{C}} \mathbf{w} \cdot (\mathbf{q}_c - \mathbf{t}_{\text{SL}} - \mathbf{t}_{\text{LG}}) \, ds = 0 \quad \forall \mathbf{w} \in \mathcal{W}. \quad (33)$$

Since

$$\mathbf{w} \cdot \mathbf{t}_{;\alpha}^\alpha = w_\alpha \sigma^{\alpha\beta}_{;\beta} + w \sigma^{\alpha\beta} b_{\alpha\beta} \quad (34)$$

and  $\mathbf{w} \cdot \mathbf{t}_I = \mathbf{w} \cdot (t_I^\alpha \mathbf{a}_\alpha) = w_\alpha t_I^\alpha$  on each  $\mathcal{S}_I$ , we obtain

$$\begin{aligned} \sum_I \left[ \int_{\mathcal{S}_I} w_\alpha \sigma^{\alpha\beta}_{;\beta} \, da - \int_{\partial\mathcal{S}_I} w_\alpha t_I^\alpha \, ds \right] + \int_{\mathcal{S}} (w \sigma^{\alpha\beta} b_{\alpha\beta} + \mathbf{w} \cdot \mathbf{f}) \, da \\ + \int_{\partial_t\mathcal{S}} \mathbf{w} \cdot \bar{\mathbf{t}} \, ds + \int_{\mathcal{C}} \mathbf{w} \cdot \mathbf{q}_c \, ds = 0, \quad \forall \mathbf{w} \in \mathcal{W}, \end{aligned} \quad (35)$$

where  $I$  denotes either LG or SL. Using the divergence theorem for curved surfaces ([23], see also [11]) and Eq. (12), this yields

$$G_{\text{int}} + G_c - G_f - G_{\text{ext}} = 0 \quad \forall \mathbf{w} \in \mathcal{W}, \quad (36)$$

with the virtual work contributions

$$\begin{aligned} G_{\text{int}} &:= \int_{\mathcal{S}} w_{\alpha;\beta} \sigma^{\alpha\beta} \, da - \int_{\mathcal{S}} w \sigma^{\alpha\beta} b_{\alpha\beta} \, da, \\ G_c &:= - \int_{\mathcal{S}} \mathbf{w} \cdot \mathbf{f}_c \, da, \\ G_f &:= \int_{\mathcal{S}} \mathbf{w} \cdot \mathbf{f}_f \, da, \\ G_{\text{ext}} &:= \int_{\mathcal{S}} \mathbf{w} \cdot \bar{\mathbf{f}} \, da + \int_{\partial_t\mathcal{S}} \mathbf{w} \cdot \bar{\mathbf{t}} \, ds + \int_{\mathcal{C}} \mathbf{w} \cdot \mathbf{q}_c \, ds. \end{aligned} \quad (37)$$

The two terms appearing in  $G_{\text{int}}$  correspond to the in-plane and out-of-plane contributions. If  $\sigma_{\text{sta}}^{\alpha\beta} = 0$ , they can be combined into the expression

$$G_{\text{int}} = \int_{\mathcal{S}} \mathbf{w}_{;\alpha} \cdot \sigma^{\alpha\beta} \mathbf{a}_\beta \, da, \quad (38)$$

see [11]. For the FE implementation in the following, both expressions for  $G_{\text{int}}$  are considered. On the other hand, using

$$\mathbf{w} \cdot \mathbf{f} = w_\alpha f^\alpha + w p \quad (39)$$

and  $\mathbf{w} \cdot \bar{\mathbf{t}} = w_\alpha \bar{t}^\alpha$ , one can also decompose the entire weak form into in-plane and out-of-plane contributions. This is considered in [11] for the case of  $\mathcal{C} = \emptyset$ . Due to the kink at  $\mathcal{C}$ , the split of the entire weak form into in-plane and out-of-plane is now unsuitable.

For physical and variational consistency, the stress tensor appearing in both terms of  $G_{\text{int}}$  should be identical. For liquids this is  $\sigma^{\alpha\beta} = \gamma a^{\alpha\beta}$ . However, as noted in Sec. 2.3, the (quasi-static) in-plane behavior of liquids is unstable. We thus use the split in (37.1) to apply the stabilized stress

$$\sigma^{\alpha\beta} = \gamma a^{\alpha\beta} + \sigma_{\text{sta}}^{\alpha\beta}, \quad (40)$$

motivated in Sec. 2.4, to the in-plane part, i.e. to the first term of Eq. (37.1). This introduces a (small) variational inconsistency. However this inconsistency only affects the in-plane behavior, which can be associated with mesh motion, but does not affect the physical out-of-plane behavior. In the computational setting a discretization error is introduced that obstructs the clear distinction between in-plane and out-of-plane behavior. Therefore the stabilization also affects the physical out-of-plane behavior. This numerical error is examined in the examples of Sec. 4. An alternative, variationally consistent stabilization procedure is proposed in Sec. 3.5 for a mesh update step that considers applying the stabilization (40) throughout (37.1).

For the following numerical examples we consider  $\bar{\mathbf{f}} = \mathbf{0}$ . Thus for hydrostatic conditions,  $f_c^\alpha = 0$  and  $f_f^\alpha = 0$ , and eqs. (37.2), (37.3) and (37.4) can be simplified using (39). In summary, the problem of Tab. 1 has thus been rewritten into the statement

$$\begin{aligned} G(\mathbf{x}, \mathbf{w}, p_c, p_v) &= G_{\text{int}}(\mathbf{x}, \mathbf{w}) + G_c(\mathbf{x}, \mathbf{w}, p_c) - G_f(\mathbf{x}, \mathbf{w}, p_v) - G_{\text{ext}}(\mathbf{x}, \mathbf{w}) = 0 \quad \forall \mathbf{w} \in \mathcal{W} \\ g_n(\mathbf{x}) &\geq 0 \quad \forall \mathbf{x} \in \mathcal{S} \\ g_v(\mathbf{x}) &= 0 \\ \mathbf{u} &= \bar{\mathbf{u}} \quad \text{on } \partial_u \mathcal{S} \end{aligned}$$

(41)

that now governs the unknown membrane configuration  $\mathbf{x} \in \mathcal{S}$ . Here, contact constraint (41.2) is still enforced pointwise  $\forall \mathcal{S}$ . If desired, one can also rewrite this equation in integral form.

### 3 Finite element discretization

The governing set of equations (41) are solved by the finite element (FE) method. Since they are composed solely by integrals over the droplet surface  $\mathcal{S}$ , only this domain needs to be discretized. A Lagrangian FE description is considered, where we denote a finite element of the reference configuration by  $\Omega_0^e$ , and its counterpart in the current configuration by  $\Omega^e$ . This discretization leads to an approximation of the geometry, denoted  $\mathcal{S}_0^h$  and  $\mathcal{S}^h$ .

#### 3.1 Finite element interpolation

The element configurations  $\Omega_0^e$  and  $\Omega^e$  are defined by the interpolation

$$\mathbf{X}^h = \mathbf{N} \mathbf{X}_e, \quad \mathbf{X}^h \in \Omega_0^e \subset \mathcal{S}_0^h, \quad (42)$$

and

$$\mathbf{x}^h = \mathbf{N} \mathbf{x}_e, \quad \mathbf{x}^h \in \Omega^e \subset \mathcal{S}^h, \quad (43)$$

where  $\mathbf{N} := [N_1 \mathbf{I}_3, \dots, N_I \mathbf{I}_3, \dots]$  is a  $(3 \times 3n_{\text{ne}})$  array of the  $n_{\text{ne}}$  shape functions  $N_I = N_I(\xi^1, \xi^2)$  of element  $\Omega_e$ .  $\mathbf{I}_3$  is the usual identity tensor in  $\mathbb{R}^3$ . The vectors

$$\mathbf{X}_e = \begin{bmatrix} \mathbf{X}_1 \\ \mathbf{X}_2 \\ \vdots \\ \mathbf{X}_{n_{\text{ne}}} \end{bmatrix} \quad \text{and} \quad \mathbf{x}_e = \begin{bmatrix} \mathbf{x}_1 \\ \mathbf{x}_2 \\ \vdots \\ \mathbf{x}_{n_{\text{ne}}} \end{bmatrix} \quad (44)$$

contain the nodal positions for the element. In the following examples, 9-noded quadrilateral elements are used based on Lagrange [24] and NURBS interpolation [25]. These elements can be conveniently related to a master element in the parameter domain  $\xi^\alpha \in [-1, 1]$ .

From (43) follows that

$$\mathbf{a}_\alpha^h = \mathbf{N}_{,\alpha} \mathbf{x}_e . \quad (45)$$

The variation  $\mathbf{w}$  is discretized in the same way as  $\mathbf{x}$ , i.e.

$$\mathbf{w}^h = \mathbf{N} \mathbf{w}_e . \quad (46)$$

In the following we omit superscript  $h$ , but imply that all quantities are approximate quantities related to  $\mathcal{S}^h$  and  $\mathcal{S}_0^h$ .

### 3.2 Discretized weak form

With approximations (42) – (46) the weak form (41.1) can be written as

$$G = \sum_{e=1}^{n_{\text{el}}} G^e , \quad (47)$$

where

$$G^e = \mathbf{w}_e^T [\mathbf{f}_{\text{int}}^e + \mathbf{f}_c^e - \mathbf{f}_f^e - \mathbf{f}_{\text{ext}}^e] , \quad (48)$$

is the contribution from element  $\Omega_e$ . Here we have identified the elemental internal force vector

$$\mathbf{f}_{\text{int}}^e = \int_{\Omega_e} \mathbf{N}_{,\alpha}^T \sigma^{\alpha\beta} \mathbf{N}_{,\beta} da \mathbf{x}_e , \quad (49)$$

according to (38), the elemental contact force vector

$$\mathbf{f}_c^e = - \int_{\Omega_e} \mathbf{N}^T f_c^\alpha \mathbf{a}_\alpha da + \int_{\Omega_e} \mathbf{N}^T p_c \mathbf{n} da , \quad (50)$$

according to (37.2), and the elemental force vectors due to the fluid forces,

$$\mathbf{f}_f^e = \int_{\Omega_e} \mathbf{N}^T f_f^\alpha \mathbf{a}_\alpha da + \int_{\Omega_e} \mathbf{N}^T p_f \mathbf{n} da , \quad (51)$$

and the external forces,

$$\mathbf{f}_{\text{ext}}^e = \int_{\Omega_e} \mathbf{N}^T \bar{f}^\alpha \mathbf{a}_\alpha da - \int_{\Omega_e} \mathbf{N}^T \bar{p} \mathbf{n} da + \int_{\Gamma_t^e} \mathbf{N}_t^T \bar{\mathbf{t}} ds + \int_{\Gamma_c^e} \mathbf{N}_t^T \mathbf{q}_c ds , \quad (52)$$

according to (37.3) and (37.4). Here  $\Gamma_t^e \subset \partial_t \mathcal{S}$  and  $\Gamma_c^e \subset \mathcal{C}$  denote the line elements along the Neuman boundary  $\partial_t \mathcal{S}$  and interface  $\mathcal{C}$ .  $\mathbf{N}_t$  is the corresponding array of shape function – for quadratic elements a  $(3 \times 9)$  array. In the examples of Sec. 4, we consider quasi-static conditions

(with  $f_f^\alpha = 0$ ) without external domain forces ( $\bar{f}^\alpha = 0$ ,  $\bar{p} = 0$ ) and Neumann tractions ( $\bar{\mathbf{t}} = \mathbf{0}$ ). In this case frictional contact forces are not supported, so that  $f_c^\alpha = 0$ .

As an alternative to (49), we can split  $\mathbf{f}_{\text{int}}^e$  into its in-plane and out-of-plane contributions

$$\begin{aligned}\mathbf{f}_{\text{inti}}^e &= \int_{\Omega_0^e} \sigma^{\alpha\beta} \left( \mathbf{N}_{,\alpha}^T \mathbf{N}_{,\beta} + \mathbf{N}^T (\mathbf{n} \otimes \mathbf{n}) \mathbf{N}_{,\alpha\beta} \right) da \mathbf{x}_e , \\ \mathbf{f}_{\text{into}}^e &= - \int_{\Omega_0^e} \sigma^{\alpha\beta} \mathbf{N}^T (\mathbf{n} \otimes \mathbf{n}) \mathbf{N}_{,\alpha\beta} da \mathbf{x}_e ,\end{aligned}\tag{53}$$

such that  $\mathbf{f}_{\text{int}}^e = \mathbf{f}_{\text{inti}}^e + \mathbf{f}_{\text{into}}^e$ . This follows from (37.1) as is shown in [11]. It is noted that the implementation of (49) is more efficient than that of (53). This can be seen from the expressions of the tangent matrix, given in App. A. As long as the stress  $\sigma^{\alpha\beta}$  is not treated differently within (53.1) and (53.2), as is the case in stabilization scheme (40), expression (49) should therefore be preferred in computations.

The original weak form (41.1) now yields the discretized version

$$\mathbf{w}^T [\mathbf{f}_{\text{int}} + \mathbf{f}_c - \mathbf{f}_f - \mathbf{f}_{\text{ext}}] = \mathbf{0} , \quad \forall \mathbf{w} \in \mathcal{W}^h .\tag{54}$$

Together with the two constraints, this yields the following set of equations to be solved at the free nodes<sup>7</sup> for the unknown discrete deformation  $\mathbf{x}$  and pressures  $p_c$ ,  $p_f$ :

$\begin{aligned}\mathbf{f}(\mathbf{x}, p_c, p_f) &:= \mathbf{f}_{\text{int}}(\mathbf{x}) + \mathbf{f}_c(\mathbf{x}, p_c) - \mathbf{f}_f(\mathbf{x}, p_f) - \mathbf{f}_{\text{ext}}(\mathbf{x}) = \mathbf{0} , \\ g_n(\mathbf{x}) &\geq 0 \\ g_v(\mathbf{x}) &= 0\end{aligned}$	(55)
--	------

The contact pressure  $p_c$ , which serves as a Lagrange multiplier to (55.2), can also be discretized within the FE setup. Here we will consider a penalty regularization that is discussed in Sec. 3.3. The discretization of the volume constraint (55.3) is discussed in [11]. Since system (55) is nonlinear, the Newton-Raphson scheme is used for its solution. The corresponding tangent matrices are given in Appendix A.

### 3.3 Contact penalty regularization

The contact pressure is determined here by a penalty regularization, i.e. we consider

$$p_c = \begin{cases} -\epsilon_n g_n , & g_n < 0 , \\ 0 , & g_n \geq 0 , \end{cases}\tag{56}$$

where  $g_n$  is the normal gap defined in (31) and  $\epsilon_n$  denotes a chosen penalty parameter. This eliminates unknown  $p_c$  and Eq. (55.2) from the above system.

### 3.4 On the application of the line load $\mathbf{q}_c$

The contact line  $\mathcal{C}$  is discretized by the line elements  $\Gamma_c^e$  (giving  $\mathcal{C}^h$ ). The FE forces on those, due to line load  $\mathbf{q}_c$ , are

$$\mathbf{f}_{\text{ext}\mathcal{C}}^e = \int_{\Gamma_c^e} \mathbf{N}_t^T \mathbf{q}_c ds .\tag{57}$$

<sup>7</sup>i.e. the remaining nodes after applying the discretized Dirichlet BC  $\mathbf{x}_I = \bar{\mathbf{x}}_I$  for nodes  $I$  on  $\partial_u \mathcal{S}^h$ .

The basis  $\{\mathbf{m}_c, \mathbf{a}_c, \mathbf{n}_c\}$  (cf. Fig. 1), required to characterize  $\mathbf{q}_c$ , is determined as follows: The tangent vector  $\mathbf{a}_c$  follows from parameterization (43), which now simplifies to

$$\mathbf{x}_c = \mathbf{N}_t \mathbf{x}_e, \quad \mathbf{x}_c \in \Gamma_c^e \subset \mathcal{C}^h. \quad (58)$$

Thus

$$\mathbf{a}_c = \frac{\partial \mathbf{x}_c}{\partial \xi} = \mathbf{N}_{t,\xi} \mathbf{x}_e. \quad (59)$$

Given  $\mathbf{a}_c$ , one can evaluate  $ds = \|\mathbf{a}_c\| d\xi$  in order to integrate (57) over  $\xi \in [-1, 1]$ . The surface normal  $\mathbf{n}_c$  is defined by the known substrate surface  $\partial\mathcal{B}$  that is treated as rigid here. During computations,  $\mathbf{n}_c$  is determined by a closest point projection of  $\mathbf{x}_c$  onto  $\partial\mathcal{B}$ . Given  $\mathbf{a}_c$  and  $\mathbf{n}_c$  we can determine  $\mathbf{m}_c$  from

$$\mathbf{m}_c = \frac{\mathbf{a}_c \times \mathbf{n}_c}{\|\mathbf{a}_c \times \mathbf{n}_c\|}. \quad (60)$$

We note that  $\mathbf{a}_c$  is orthogonal to  $\mathbf{n}_c$  as Fig. 1 shows. But this is only true at the final solution and not necessary during the numerical procedure that takes us there. We therefore cannot assume  $\mathbf{a}_c \perp \mathbf{n}_c$  when deriving the tangent matrix of  $\mathbf{f}_{\text{ext}\mathcal{C}}^e$ ; see Appendix A.

### 3.5 Stabilization of liquid membranes

We now discuss the computational adaption of the stabilization schemes introduced in Sec. 2.4. Two different approaches are proposed:

**First approach:** Following description (27), the internal force in (55),  $\mathbf{f}_{\text{int}}^e$ , is now replaced by

$$\mathbf{f}_{\text{int,stab}}^e = \mathbf{f}_{\text{int}}^e(\sigma_{\text{liq}}^{\alpha\beta}) + \mathbf{f}_{\text{int}}^e(\sigma_{\text{sta}}^{\alpha\beta}), \quad (61)$$

where  $\sigma_{\text{liq}}^{\alpha\beta} := \gamma a^{\alpha\beta}$ . Depending on the formulation of  $\sigma_{\text{sta}}^{\alpha\beta}$ , this idea is denoted as scheme ‘A’ or scheme ‘a’. For comparison we also examine the scheme

$$\mathbf{f}_{\text{int,stab}}^e = \mathbf{f}_{\text{int}}^e(\sigma_{\text{liq}}^{\alpha\beta} + \sigma_{\text{sta}}^{\alpha\beta}), \quad (62)$$

based on (26). This is then denoted as scheme ‘a-t’.

**Second approach:** An different stabilization scheme is given by the following two-step procedure. We first solve (55) considering expression (62) in order to update the FE mesh. We then solve the physically correct problem with

$$\mathbf{f}_{\text{int,unstab}}^e = \mathbf{f}_{\text{int}}^e(\sigma_{\text{liq}}^{\alpha\beta}) \quad (63)$$

inside (55). Since this is unstable, i.e. the stiffness matrix

$$\mathbf{K} = \frac{\partial \mathbf{f}}{\partial \mathbf{u}} \quad (64)$$

is singular, the linearized system (at load step  $k+1$ )

$$\mathbf{f}(\mathbf{u}_{k+1}) \approx \mathbf{f}(\mathbf{u}_k) + \mathbf{K}(\mathbf{u}_k) \Delta \mathbf{u}_{k+1} = \mathbf{0} \quad (65)$$

needs to be reduced to a stable subsystem. This can be achieved by considering the reduction

$$\mathbf{u}_{\text{red}} = \mathbf{P} \mathbf{u}, \quad (66)$$

where  $\mathbf{P}$  denotes the projection matrix

$$\mathbf{P} := \begin{bmatrix} \mathbf{n}_1^T & \mathbf{0}^T & \dots & \mathbf{0}^T \\ \mathbf{0}^T & \mathbf{n}_2^T & \dots & \mathbf{0}^T \\ \vdots & \vdots & \ddots & \vdots \\ \mathbf{0}^T & \mathbf{0}^T & \dots & \mathbf{n}_{n_{\text{no}}}^T \end{bmatrix} \quad (67)$$

that is based on the surface normal  $\mathbf{n}_I$  at the FE nodes (or control points, respectively)  $\mathbf{x}_I$ ,  $I = 1, \dots, n_{\text{no}}$ .  $\mathbf{u}_{\text{red}}$  thus only contains the normal components of  $\mathbf{u}$ . With this, system (65) is reduced to

$$\mathbf{K}_{\text{red}} \Delta \mathbf{u}_{\text{red}} = -\mathbf{f}_{\text{red}}, \quad \text{with } \mathbf{K}_{\text{red}} = \mathbf{P} \mathbf{K} \mathbf{P}^T, \quad \mathbf{f}_{\text{red}} = \mathbf{P} \mathbf{f}, \quad (68)$$

which is stable. Once  $\mathbf{u}_{\text{red}}$  is found,  $\mathbf{u}$  is determined from  $\mathbf{u} = \mathbf{P}^T \mathbf{u}_{\text{red}}$ . Since this solution only provides an update in the out-of-plane direction, the preceding step for the mesh update is required to provide tangential updates of  $\mathbf{u}$ . In principle, such an update will not be required at every load step. For Lagrange FE, the interpolation is not  $C^1$ -smooth at the element boundaries. In this case the normals are defined by averaging the normal of adjacent elements. For NURBS FE, the interpolation may be  $C^1$  everywhere, but the control points do not lie on the surface. One can then project them onto the surface to obtain a corresponding normal. This would need to be done at every load step, due to the deformation. It turns out that this is unnecessary, since the scheme works very well for an approximation of  $\mathbf{n}_I$ . For efficiency, we will therefore only compute the projected control points in the initial configuration, and then evaluate  $\mathbf{n}_I$  at those locations (convected to the current configuration). During computations we take  $\mathbf{n}_I$  from the previous step, to avoid further linearizing (68). The second stabilization scheme is denoted as scheme ‘P’.

## 4 Numerical examples

This section presents six examples that focus on the various aspects of the proposed formulation and thus demonstrate the capabilities of the presented FE model. The examples are also used to assess the four stabilization schemes given in Sec. 3.5. Both quadratic Lagrange elements and quadratic NURBS-based elements are considered.

### 4.1 Surface curvature example: Stretched liquid film

The first example considers a liquid film stretched between two rigid rings. Contributions  $G_c$ ,  $G_f$  and  $G_{\text{ext}}$  are considered to be zero in (41), such that the film is only governed by the surface curvature term. The rings have radius  $L_0$ . The free liquid film has one liquid-gas interface on each side such that the membrane surface tension is  $\gamma = 2\gamma_{\text{LG}}$ . Due to symmetry, only 1/8 of the problem is modeled computationally, considering an initial width of  $H = 0.1 L_0$ . Fig. 3 shows this reference configuration, which itself is not in equilibrium. To stretch the film, a displacement  $\bar{u}$  is applied such that the final width is  $h = H + \bar{u}$ . For low values of  $\bar{u}$  (Fig. 3b) the film forms a meniscus. The analytical solution of this meniscus can be obtained from variational calculus (by minimization of the surface area) as

$$r(y) = c \cosh \frac{y}{c}, \quad (69)$$

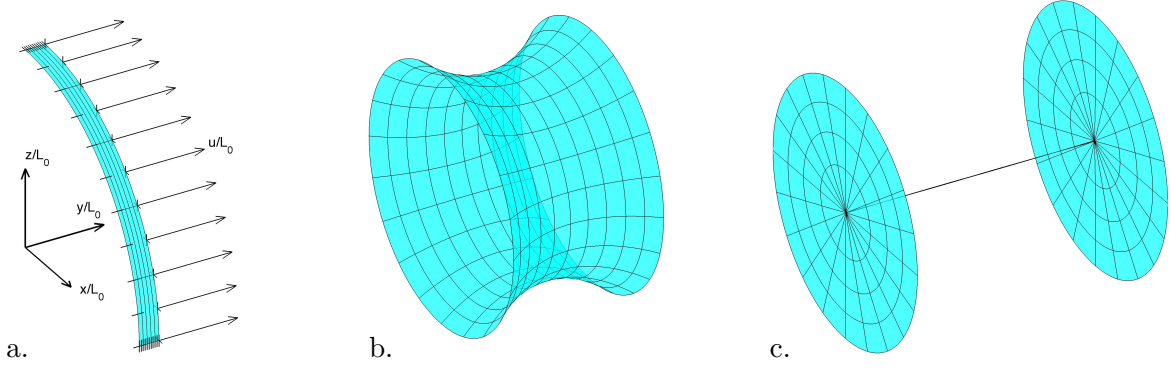


Figure 3: Stretched liquid film: a) Reference configuration; b) configuration for  $\bar{u} = 0.5 L_0$ ; c) configuration for  $\bar{u} = 0.9 L_0$ .

where the constant  $c = r(0)$  is obtained from the condition  $r(h) = L_0$ . The surface area is then given by

$$a = \int_{\mathcal{S}} da = 4\pi \int_0^h r \sqrt{1 + r'^2} dy = 2\pi c \left( h + c \sinh \frac{h}{c} \cosh \frac{h}{c} \right), \quad (70)$$

and the enclosed volume becomes

$$V = 2 \int_0^h \pi r^2 dy = \pi c^2 \left( h + c \sinh \frac{h}{c} \cosh \frac{h}{c} \right). \quad (71)$$

For large values of  $\bar{u}$  the configuration shown in Fig. 3c is energetically more favorable. It is possible to obtain that solution computationally with quadratic Lagrange elements. This is quite remarkable as several elements have degenerated into lines, as the figure shows. This second solution is characterized by the area  $a = 2\pi L_0^2$ .

As Fig. 4 shows, the computational result follows the analytical result (70) up to  $\bar{u} = 0.69 L_0$ , and then abruptly switches to the result  $a = 2\pi L_0^2$ . According to theory, the stress state within

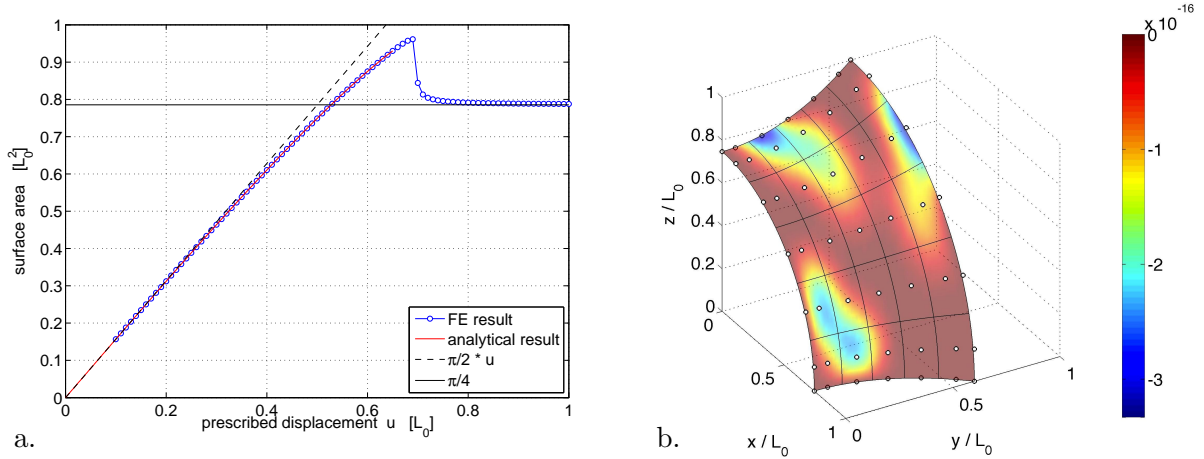


Figure 4: Stretched liquid film: a) surface area ( $\times 1/8$ ) vs. prescribed deformation  $h = H + \bar{u}$ ; b) computational surface tension error  $|(\sigma_\alpha^\alpha - 2\gamma)|$  for N2 ‘P’ at  $\bar{u} = 0.5 L_0$ .

the membrane is constant, see Sec. 2.2. Using a standard stress recovery scheme<sup>8</sup> this stress

<sup>8</sup>based on least square minimization between interpolated and quadrature point stresses [26]

state is recovered to machine precision as Fig. 4b shows. This is also the case for all the following examples.

Next, we examine the computational accuracy of the meniscus shape for the four different stability formulations, ‘A’, ‘a’, ‘a-t’ and ‘P’, introduced earlier. We therefore look at the  $L_2$ -error norm between the FE result and the analytical result (69). Two different FE types are considered: quadratic Lagrange (L2) and quadratic NURBS (N2) elements. Fig. 5 shows the convergence w.r.t. the mesh discretization. This figure shows that the N2 discretization is much

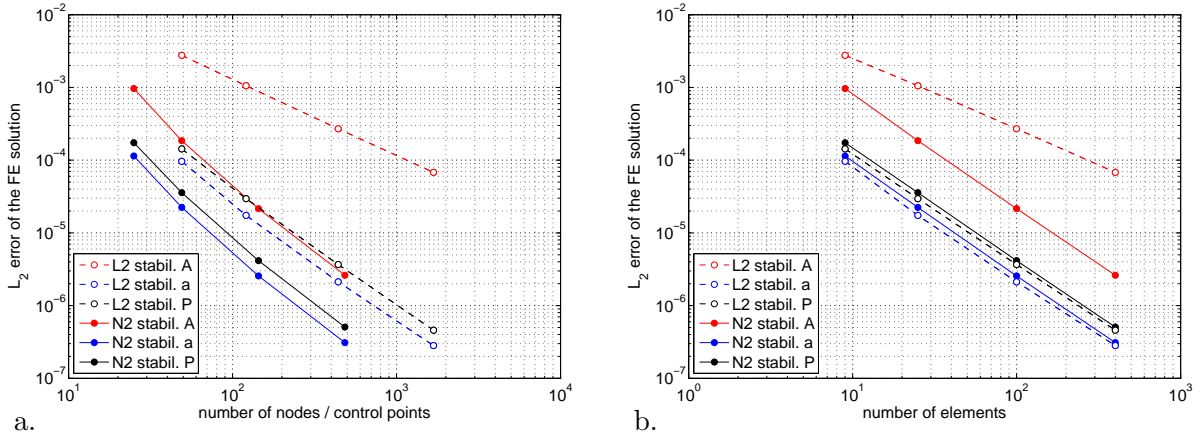


Figure 5: Stretched liquid film:  $L_2$ -error of the film shape in dependence of a) FE nodes and b) element number. For scheme ‘P’  $n_t = 50$  load steps have been used; for scheme ‘a’  $n_t = 1000$  steps are used for L2 and  $n_t = 100$  for N2 FE. For scheme ‘A’  $\mu = 0.1 \gamma$ ; otherwise  $\mu = \gamma$ .

more accurate than the L2 discretization. This is attributed to the fact that a  $C^1$ -continuous surface allows a much more accurate definition of in-plane and out-of-plane directions. It is further seen that the new stabilization schemes proposed in this work – ‘a’ and ‘P’ – perform best and are of similar accuracy. The old scheme, ‘A’, is the least accurate, but it still converges. For N2 finite elements ‘A’ is still as accurate as the best L2 cases.

Fig. 6 shows the convergence w.r.t. the temporal discretization  $n_t$  (i.e. the number of load steps). This figure shows that schemes ‘a’ and ‘a-t’ improve with  $n_t$ . Scheme ‘P’, on the other hand, does not show this property. For small  $n_t$ , it even increases with  $n_t$ . However, for small  $n_t$ , the overall solution scheme may not converge anymore so that this advantage may not be exploited in general. Due to this, we can argue that schemes ‘a’ and ‘P’ are equally accurate, which is why we will mostly focus on those two schemes in the following examples. Fig. 6b confirms earlier findings [11]. In all cases the convergence saturates at the mesh error, which, for  $n_{el} = 5^2$  elements, lies around  $10^{-5}$ .

## 4.2 Pressure example: Inflated liquid film

The second example extends the previous example by surface pressure (term  $G_f$ ) and the corresponding volume constraint. Due to their superiority, we now only consider schemes ‘a’ and ‘P’. Both quadratic Lagrange and quadratic NURBS FE are used. We consider the configuration of Fig. 3b and inflate it as shown in Fig. 7. The volume of this starting configuration is  $V_0 \approx 2.61 L_0^3$ , according to (71). During inflation the liquid membrane attains two special solutions: a cylinder with radius  $r_C = L_0$  and volume  $V_C = 1.2\pi L_0^3$  and a capped sphere with radius

$$r_S = \sqrt{1 + 0.6^2} L_0 \quad (72)$$

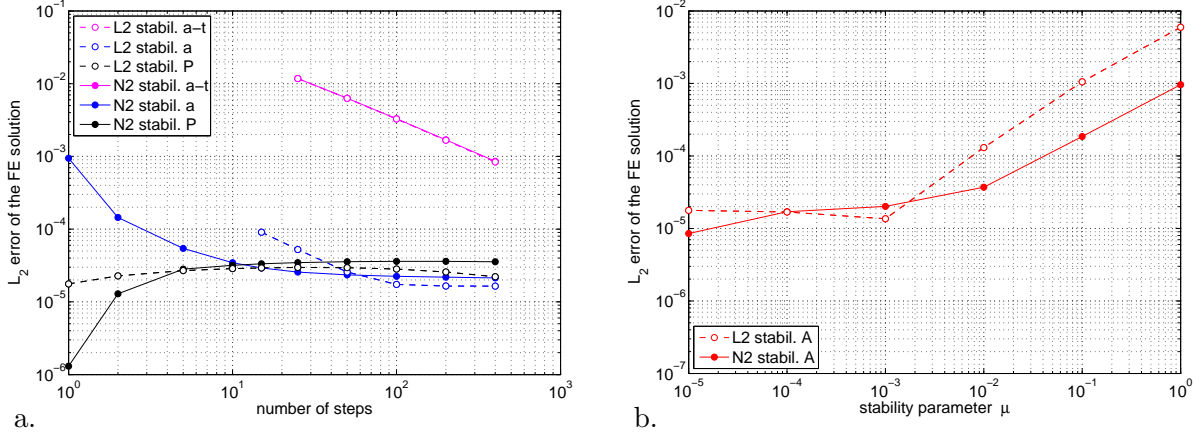


Figure 6: Stretched liquid film:  $L_2$ -error of the film shape in dependence of a) the number of load steps, and b) stability parameter  $\mu$ . Here  $n_{el} = 5^2$ . The solution according to scheme ‘A’ does not depend on  $n_t$ .

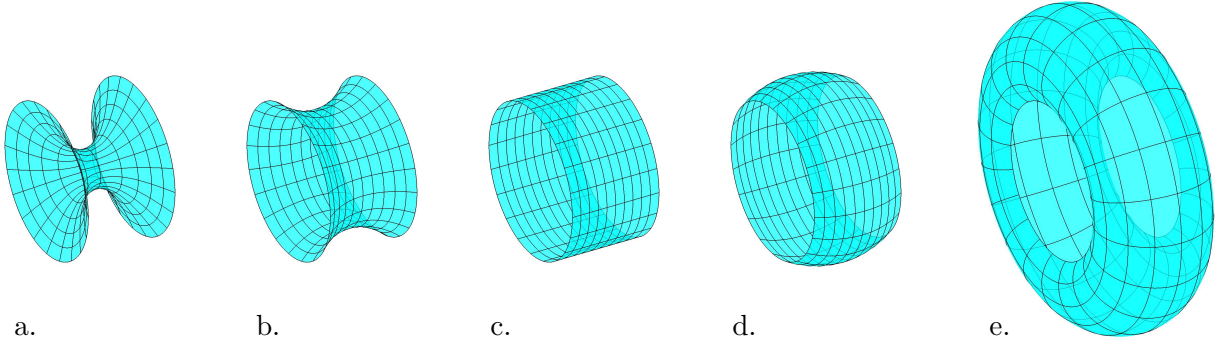


Figure 7: Inflated liquid film: Configuration for a prescribed volume of a)  $V = V_A$ , b)  $V = V_0$  (initial configuration), c)  $V = V_C$ , d)  $V = V_S$  and e)  $V = V_B$ .

and volume

$$V_S = 4\pi/3r_S^3 - \pi a_S(1 + a_S^2/3), \quad \text{with } a_S = r_S - 0.6L_0. \quad (73)$$

At these two configurations the pressure is known analytically as  $p_C = \gamma/r_C$  and  $p_S = 2\gamma/r_S$ , which is used in the following to analyze the numerical error. Computationally an inflation up to  $V_B = 16L_0^3$  has been considered. Deflation can also be considered. The computations run robustly up to about  $V_A = 1.12L_0^3$ . The pressure-volume curve for the inflation and deflation process is shown in Fig. 8.

Next, we examine the computational error in the pressure for  $V = V_C$  and  $V = V_S$ , defined as  $|1 - p^h/p|$ . This is shown in Figs. 9 and 10. The convergence behavior for decreasing mesh size (Fig. 9) is similar to that of the previous example. Again N2 FE are more accurate, while schemes ‘a’ and ‘P’ are quite close. The convergence behavior for decreasing load steps (Fig. 10) shows that scheme ‘a’ decreases, while scheme ‘P’ remains unaffected. For N2 FE, scheme ‘a’ can beat scheme ‘P’ for a very high number of load steps.

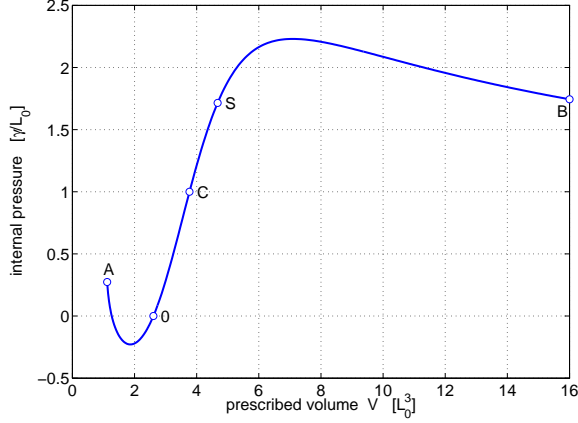


Figure 8: Inflated liquid film: pressure-volume relation; marked are the five configurations from Fig. 7.

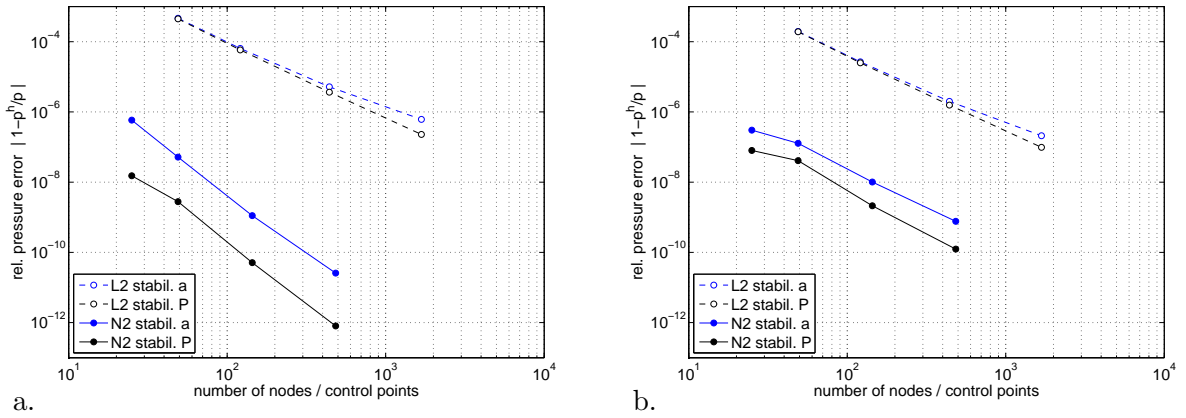


Figure 9: Inflated liquid film: relative pressure error in dependence of the FE nodes / control points for: a)  $V = V_C$ ; b)  $V = V_S$ . Here  $n_t = 100$  for L2 ‘a’ and 50 for all other schemes.

### 4.3 Surface contact example: Droplet under gravity

The third example includes surface contact (including term  $G_c$  and the corresponding contact constraint). For that we consider contact between a liquid, incompressible droplet and a flat surface due to gravity, taking a contact angle of  $\theta_c = 180^\circ$  and considering the case  $\gamma_{SL} - \gamma_{SG} = \gamma_{LG} := \gamma$ . Fig. 11 shows the initial configuration (a sphere with radius  $R_0$ ) and the deformed configuration. Gravity acts on the internal medium leading to hydrostatic pressure (20). Here, we consider  $\mathbf{g} = -[0, 0, g]^T$  with  $\rho g = 2\gamma/R_0^2$ . This loading is applied in  $n_t$  load steps. The penalty method (56) is used for contact. We consider stability schemes ‘A’, ‘a’ and ‘P’ for L2 and N2 finite elements. Scheme ‘A’ is included here, since a similar scheme is used for this problem in [11]. The meshes for both L2 and N2 discretizations look as is shown in Fig. 11. Four patches are used for the N2 discretization. It is noted, that during deformation, the N2 discretization is not  $C^1$ -continuous anymore at the patch boundaries. The contact surface of the droplet is shown in Fig. 11b. The contact pressure is constant and (as noted in (18)) equal to the internal fluid pressure at the bottom, which is  $p_f = 3.571 \gamma/R_0$ . The radius of the contact surface thus is  $r_c = \sqrt{4/3 R_0^3 \rho g / p_f} = 0.864 R_0$ , which agrees with the computational result.

Tab. 2 shows the computational parameters considered for the different FE meshes. For scheme

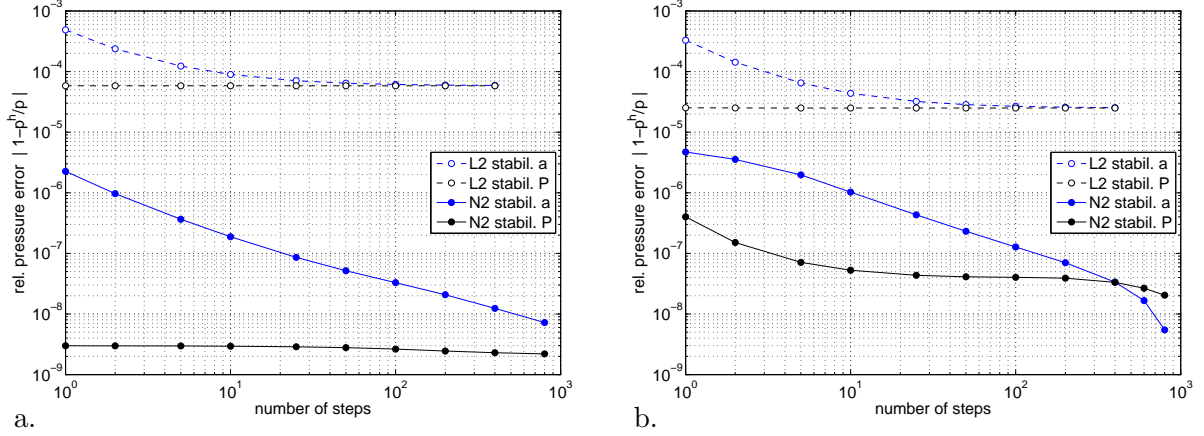


Figure 10: Inflated liquid film: relative pressure error in dependence of the number of load steps  $n_t$ : a)  $V = V_C$ ; b)  $V = V_S$ . Here  $n_{el} = 5^2$ .

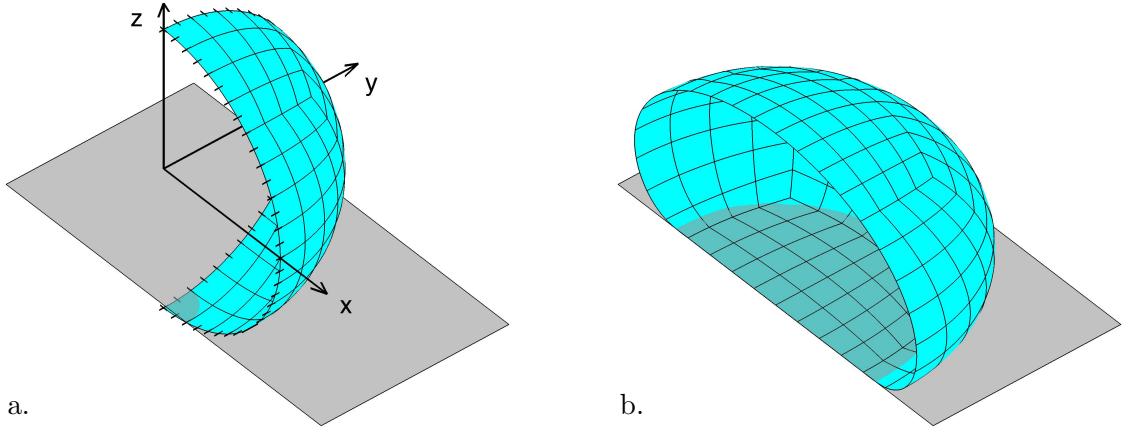


Figure 11: Droplet contact for  $\theta_c = 180^\circ$ : a) initial configuration with boundary and symmetry conditions, considering  $n_{el} = 96$  quadratic Lagrange (L2) FE; b) deformed configuration for  $\rho g = 2\gamma/R_0^2$ .

‘a’,  $n_t = 10m$ , for the other schemes,  $n_t = 10$  steps have been used for all meshes. The mesh for  $m = 64$  is used as an accurate reference result for the convergence plots shown in Fig. 12. Here the error in the fluid pressure  $p_f$  (Fig. 12a) and the contact penetration (Fig. 12b) is shown. The second figure essentially shows the closing of the contact gap with increasing penalty parameter. Fig. 12a shows that the N2 results are not always better than the L2 results, as is the case in the previous examples. Also the accuracy ordering ‘P’-‘a’-‘A’ is not always observed here either. It is further seen that the error does not decrease monotonically. The reason for this outcome is (most likely) caused by the contact boundary, where an active set change of single contact quadrature points can make a large difference.<sup>9</sup> In the contact example of Sec. 4.4 this problem is absent.

<sup>9</sup> $3 \times 3$  contact quadrature points are considered per element.

$m$	$n_{\text{el}} = 6 m^2$	$n_{\text{no L2}}$	$n_{\text{no N2}}$	$\epsilon_n = 250 m^2 \gamma / R_0$
1	6	33	28	250
2	24	113	60	1000
4	96	417	160	4000
8	384	1601	504	16000
16	1536	6273	1768	64000
32	6144	24833	6600	256000
64	24576	98817	25480	1024000

Table 2: Droplet contact: computational parameters (number of elements  $n_{\text{el}}$ , number of nodes  $n_{\text{no}}$  and contact penalty parameter  $\epsilon_n$ ) for the quarter mesh of Fig. 11a.

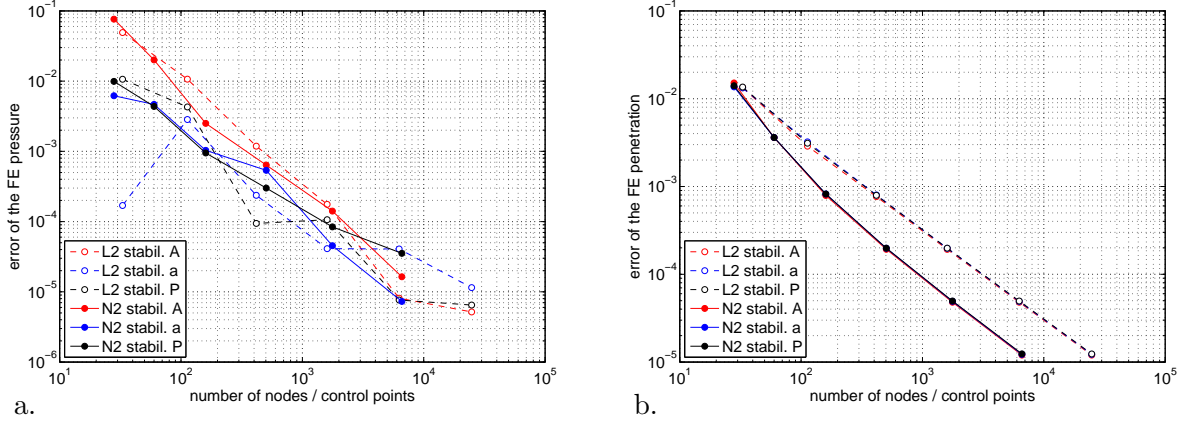


Figure 12: Droplet contact for  $\theta_c = 180^\circ$ : a) error of the internal pressure in dependence of the number of nodes/control points; b) contact penetration error at the center.

#### 4.4 Line contact example: Attached liquid droplet

The fourth example considers the previous setup and includes distinct contact angles ( $\theta_c < 180^\circ$ ) by including contribution (57) in the weak form. In this case we have both line and surface contact. The following three cases are studied:

**1. Application of  $\mathbf{q}_c$ :** One way to obtain the final solution is by a step-wise application of the line load  $\mathbf{q}_c$ , as is shown in Fig. 13. Once the full load is applied, we get the desired (physical) solution, here for  $\theta_c = 90^\circ$  and zero gravity ( $\rho g = 0$ ). Without gravity the droplet shape is spherical, such that the pressure can be computed analytically, and used to evaluate the numerical error, which is done in Fig. 14. Given the initial droplet volume  $V = 4\pi R_0^3/3$  and the contact angle  $\theta_c$ , the inside pressure is

$$p = 2\gamma/r, \quad (74)$$

where  $r$  is the radius of the current sphere, given as

$$r = (1 - f(\theta_c))^{-1/3} R_0, \quad (75)$$

with

$$f(\theta_c) = (2 + 3 \cos \theta_c - \cos^3 \theta_c)/4. \quad (76)$$

The error plots of Fig. 14 show the convergence behavior for increasing spatial and ‘temporal’ refinement, considering stability schemes ‘a’ and ‘P’ for L2 and N2 elements. At the contact line

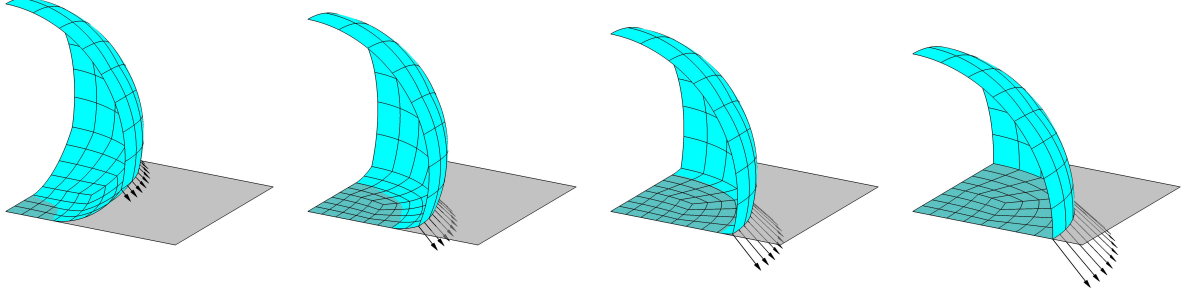


Figure 13: Droplet contact for  $\theta_c = 90^\circ$ : Intermediate configurations for  $\{1/4, 1/2, 3/4, 1\} \times \mathbf{q}_c$ . The contact surface during this transition is determined by a contact algorithm based on (56).

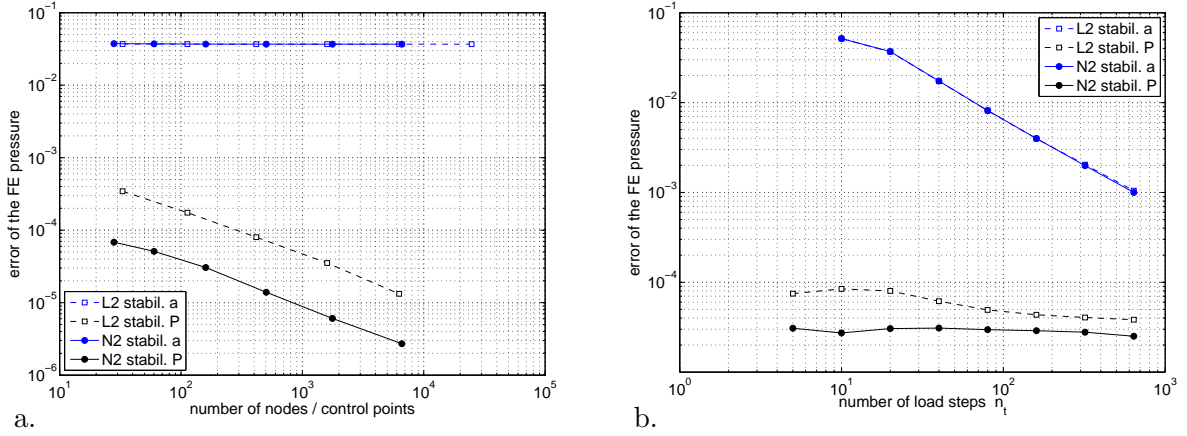


Figure 14: Droplet contact for  $\theta_c = 90^\circ$ : Pressure convergence with increasing spatial (a. with  $n_t = 20$ ) and ‘temporal’ resolution (b. with  $m = 4$ ). The parameters of Tab. 2 are used.

$\mathcal{C}$ , no unique surface normal exists, so that it becomes necessary to revisit stabilization scheme ‘P’. One possibility is to consider an averaged normal within (67). However, this turns out to be inaccurate. It also ignores the physical situation at  $\mathcal{C}$ : Due to the surface kink, the liquid membrane is naturally stabilized in the two out-of-plane directions of the adjacent surfaces. An instability therefore only remains along  $\mathcal{C}$ . We thus modify the projection matrix into

$$\mathbf{P} := \begin{bmatrix} \ddots & \ddots & \vdots & \vdots & \ddots \\ \ddots & \ddots & \mathbf{0}^T & \mathbf{0}^T & \dots \\ \dots & \mathbf{0}^T & \mathbf{n}_{I-}^T & \mathbf{0}^T & \dots \\ \dots & \mathbf{0}^T & \mathbf{n}_{I+}^T & \mathbf{0}^T & \dots \\ \dots & \mathbf{0}^T & \mathbf{0}^T & \ddots & \ddots \\ \ddots & \vdots & \vdots & \ddots & \ddots \end{bmatrix} \quad \forall \mathbf{x}_I \in \mathcal{C}^h, \quad (77)$$

where  $\mathbf{n}_{I-}$  and  $\mathbf{n}_{I+}$  denote the normals of the two adjacent surfaces at node  $\mathbf{x}_I \in \mathcal{C}^h$ . This procedure yields the excellent accuracy shown in Fig. 14.<sup>10</sup> In this example scheme ‘P’ performs much better than scheme ‘a’. For scheme ‘a’, the pressure does not even improve with mesh refinement. Comparing the L2 and N2 discretization, one can find slightly better results for N2. Since the difference is not large, we use L2 elements for the following two cases.

<sup>10</sup>In this example the projection step of scheme ‘P’ is only applied once at the end.

**2. Varying  $\theta_c$ :** Given the previous solution (Fig. 13), we now consider varying the contact angle  $\theta_c$  that defines the direction of  $\mathbf{q}_c$  according to (30). This is shown in Fig. 15. The

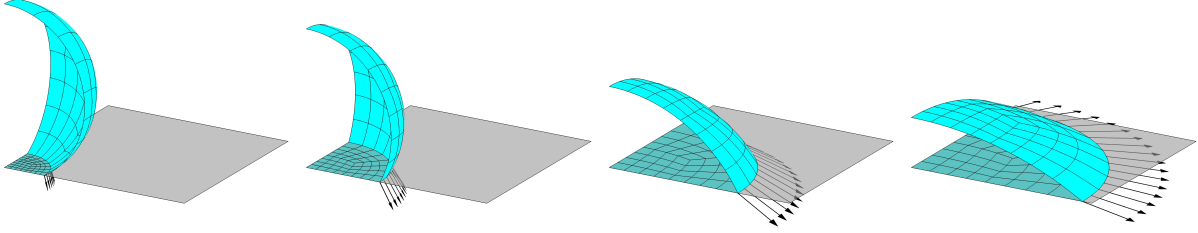


Figure 15: Attached liquid droplet: Contact angle transition,  $\theta_c = 150^\circ, 120^\circ, 60^\circ, 30^\circ$  (left to right), starting from  $\theta_c = 90^\circ$  (Fig. 13).

accuracy of these solutions is studied in Fig. 16. It is seen that scheme ‘P’ follows the exact solution (74) much closer than scheme ‘a’, even though larger load steps are taken ( $5^\circ$  vs.  $2^\circ$ ). On the other hand, scheme ‘a’ runs more robustly for this problem: scheme ‘P’ is only able to cover the range  $25^\circ \leq \theta_c \leq 95^\circ$  from the starting value  $90^\circ$ , while scheme ‘a’ is able to cover the entire range. A difficulty in scheme ‘P’ is the mesh update in the vicinity of  $\mathcal{C}$ , which is seen more clearly in the next test case.

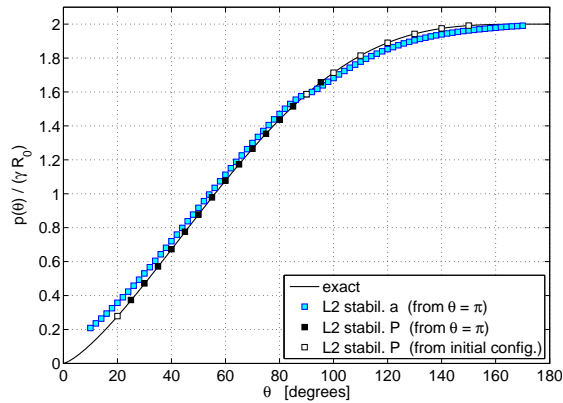


Figure 16: Attached liquid droplet: Pressure dependence on the contact angle for various stabilization schemes. The mesh data for  $m = 4$  is taken (see Tab. 2).

**3. Increasing the gravity loading:** The last case considers increasing the fluid load  $\rho g R_0^2 / \gamma$ , which can be viewed as increasing the body force  $\rho g$ , decreasing the surface tension  $\gamma$ , or increasing the scale  $R_0$ . An example is shown in Fig. 17. Since  $\theta_c$  is fixed, the line force  $\mathbf{q}_c$  remains unchanged (for fixed  $R_0$ ). But the overall force exerted along  $\mathcal{C}$  increases since  $\mathcal{C}$  stretches as the fluid load increases. Fig. 17 shows that the FE mesh deforms strongly in the vicinity of  $\mathcal{C}$ . This can affect the robustness of scheme ‘P’. Therefore we restrict ourselves to scheme ‘a’ in the remaining two examples.

#### 4.5 Curved surface contact example: Attached liquid film

In the previous two examples contact with flat surfaces was considered. To generalize this setting, we now consider contact with a curved surface. As an example we consider contact

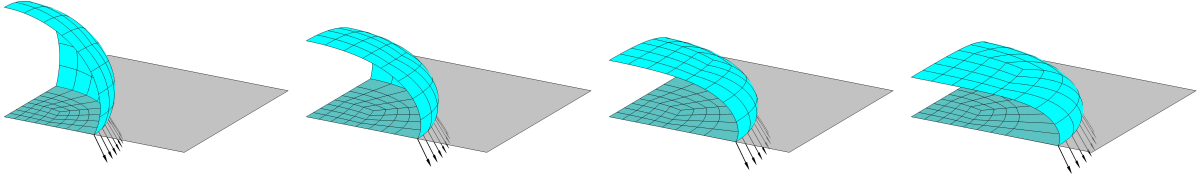


Figure 17: Attached liquid droplet: Gravity sweep for  $\theta_c = 120^\circ$  and  $\rho g = \{1, 4, 8, 16\} \gamma/R_0^2$  (left to right). The case for  $\theta_c = 120^\circ$  and  $\rho g = 0$  is contained in Fig. 15.

between a liquid sheet and a single asperity, defined by

$$z(r) = z_0 \exp\left(-\frac{r^2}{h^2}\right), \quad r^2 = x^2 + y^2. \quad (78)$$

The computational setup for the liquid film and the asperity geometry are shown in Fig. 18. The film is modeled as a flat sheet with dimension  $4L_0 \times 4L_0$ , located at  $z = L_0$ . The outer

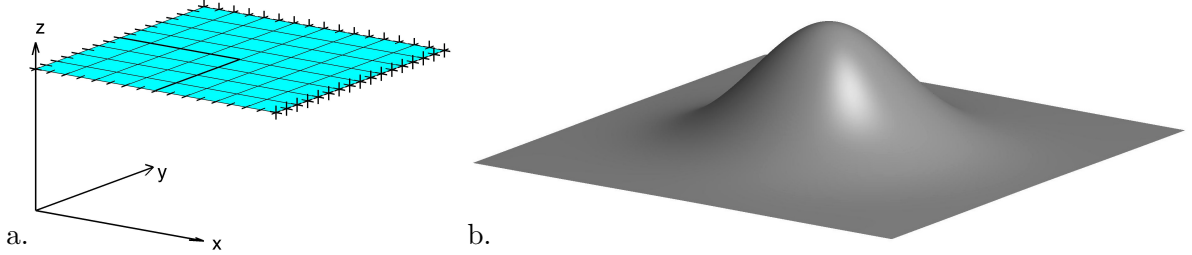


Figure 18: Attached liquid film: a) computational setup (quarter system); b) asperity surface.

boundary is considered fixed. Due to symmetry only a quarter of the system is modeled – considering appropriate symmetry boundary conditions along the center lines. 64 L2 finite elements, stabilized by scheme ‘a’, are used to discretize the quarter sheet. Various contact angles will be considered by applying the line load  $\mathbf{q}_c$  along the bold line marked in Fig. 18. This choice for  $\mathcal{C}$  leads to a degenerated mesh in the deformed configuration, as is shown below. This is chosen deliberately in order to test the FE formulation. For the asperity we consider  $z_0 = L_0$  and  $h = 0.85 L_0$ . The surface tension of the free liquid sheet is taken as  $\gamma_{LG} = \gamma/2$ , for the substrate surface we consider  $\gamma_{SL} - \gamma_{SG} = \gamma/2$ . The contact penalty parameter is taken as  $\epsilon_n = 16000 \gamma/L_0^2$ . First, a contact angle of  $\theta_c = 90^\circ$  is applied by increasing  $\mathbf{q}_c$  (as in the example of Fig. 13). Then  $\theta_c$  is varied as in the example of Fig. 15. We thus obtain the (deformed) configurations shown in Fig. 19. Due to the chosen penalty regularization, some FE penetrate into the asperity. This leads to the visualization artefacts shown in the figure. Very large mesh degeneration occurs along the contact line, due to the initial choice of the contact line. This does not lead to any computational difficulties here. A different choice, as well as remeshing procedures, will get rid of the mesh degeneration. The examples show that large changes occur between 90 and 87 degrees, which lie in the nature of this problem. In principle, a specific combination of surface roughness and contact angle parameters may lead to instabilities in computations that would require continuation, e.g. arc-length, methods. Overall it may be said that the proposed FE formulation handles this example, involving curved surface contact, nicely.

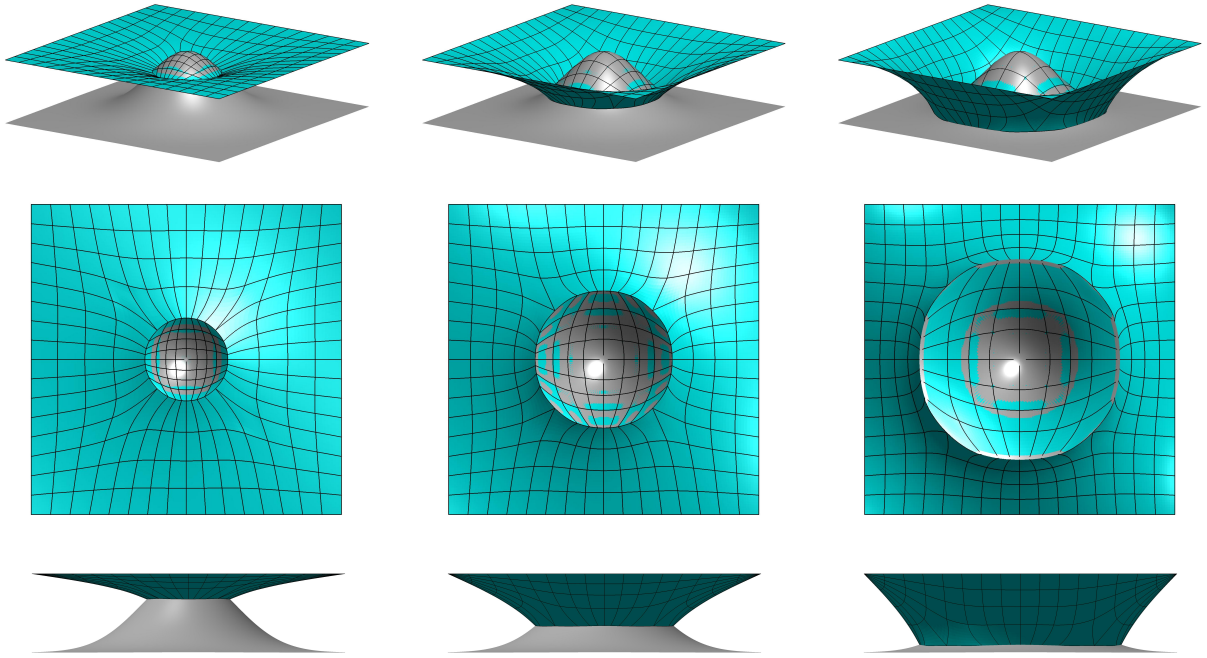


Figure 19: Attached liquid film: Contact angles  $\theta_c = 120^\circ$  (left),  $90^\circ$  (middle),  $87^\circ$  (right).

#### 4.6 Coupled contact example: Immiscible contact between two droplets

The last example considers contact between two immiscible liquid films. The example consists of a spherical droplet with initial radius  $R_0$  that sits on top of a spherical droplet with initial radius  $2R_0$ . The bottom droplet is in contact with a rigid plane. The media inside both droplets is incompressible, but only the upper droplet is affected by gravity in this example. In this setting, the lower droplet may also be viewed as a bubble filled by an incompressible gas. The surface tension of the various interfaces is chosen as follows: droplet-gas:  $\gamma_{DG} = \gamma$ , droplet-bubble:  $\gamma_{DB} = 3\gamma/2$ , bubble-gas:  $\gamma_{BG} = \gamma/2$ , bubble-substrate:  $\gamma_{BS} - \gamma_{SG} = \gamma/2$ . In consequence, the surface tension within all finite elements is  $\gamma$  and all contact angles remain  $180^\circ$ . The deformation of the two droplets, for various values of  $\rho g$ , is shown in Fig. 20. The

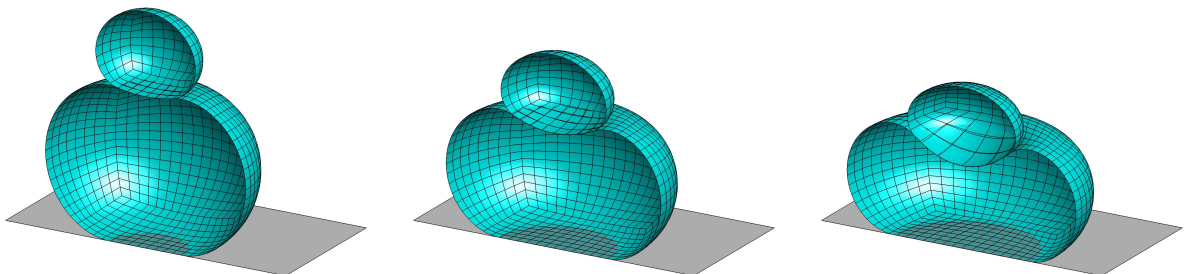


Figure 20: Droplet-droplet contact: Contact deformation for  $\rho g = \{0.5, 1.2, 2.0\}\gamma/R_0^2$  (left to right) considering  $\theta_c = 180^\circ$ .

computational setup and boundary conditions are similar to those considered in the example

of Fig. 11. Modeling only a quarter of the system, 96 L2 elements are used to discretize the droplet, and 384 L2 elements are used to discretize the bubble. Stabilization scheme ‘a’ is used. The contact between the two deforming surfaces is computed according to the two-half-pass algorithm [27]. Therefore, a contact penalty parameter of  $\epsilon_n = 1000\gamma/R_0$  is chosen. The right hand side of Fig. 20 shows that the finite elements on the contact surface are stretched strongly. But note that this does not have any physical meaning, as the in-plane mesh deformation is unrelated to the constant stress state of liquid membranes. The proposed membrane contact formulation also handles this last example without any difficulties.

## 5 Conclusion

This paper presents a new and general computational formulation for the analysis of liquid membranes and their contact behavior. The formulation is based on a general theoretical description in the framework of membrane theory in curvilinear coordinates. Two new stabilization schemes, denoted schemes ‘a’ and ‘P’, are proposed in order to circumvent the in-plane instability for quasi-static conditions. The new schemes are compared to two older schemes, that are denoted schemes ‘A’ and ‘a-t’. Suitable conditions to describe both surface and line contact are formulated. The governing equations are presented both in strong and weak form. The discretization of the latter is derived in the framework of Galerkin-type finite elements. Particular attention is placed on the discretization of the contact line load and the stabilization schemes. The formulation admits isogeometric FE discretizations, which are considered here. Altogether six numerical examples are studied to test various aspects of the proposed liquid membrane formulation. These are surface curvature, surface pressure, surface contact, line contact, curved surface contact and coupled contact.

The examples demonstrate that the formulation is able to handle all these aspects accurately, robustly and efficiently. They show that scheme ‘P’ tends to be more accurate than scheme ‘a’, which in turn is more accurate than schemes ‘a-t’ and ‘A’. However, scheme ‘a’ behaves more robust for contact lines than the current version of scheme ‘P’. The examples further show that NURBS-based isogeometric FE tend to be more accurate than Lagrange FE.

Even though a large range of applications are captured by the current formulations, there are still more aspects that should be examined in future work. These are a deformable substrate body  $\mathcal{B}$ , algorithms for contact angle hysteresis, contact pinning (i.e. stiction) and sliding, an improvement of stabilization scheme ‘P’, liquid-liquid contact with line contact, and the fluid flow within the membrane film and the enclosed media. Some aspects are addressed in the theoretical work of Sauer [22]. But corresponding computational formulations are still lacking in this framework.

## A Finite element linearization

In order to employ the Newton-Raphson scheme, system (55) needs to be linearized, leading to the tangent matrix of the system. Some aspects of this have been discussed in [11], and so we will only provide details for the new parts. In [22] we have discussed the linearization for the continuous case, disregarding the discretization. Therefore some of the following results can be obtained by discretizing the linearization of [22], simply by discretizing the changes  $\Delta\mathbf{x}$  and  $\Delta\mathbf{a}_\alpha$  appearing in the continuous setting by  $\Delta\mathbf{x}^h = \mathbf{N}\Delta\mathbf{x}_e$  and  $\Delta\mathbf{a}_\alpha^h = \mathbf{N}_{,\alpha}\Delta\mathbf{x}_e$  according to (43) and (45).

## A.1 Tangent matrix associated with $\mathbf{f}_{\text{int}}^e$

We first take a look at the contribution coming from the internal virtual work. This leads to the elemental force  $\mathbf{f}_{\text{int}}^e$  that can be split according to (53). Before deriving the tangent associated with the split, we summarize the tangent for  $\mathbf{f}_{\text{int}}^e$  derived in [11].

The linearization of the stress  $\tau^{\alpha\beta} = J\sigma^{\alpha\beta}$  is characterized by the change [22]

$$\Delta\tau^{\alpha\beta} = c^{\alpha\beta\gamma\delta} \mathbf{a}_\gamma \cdot \mathbf{N}_{,\delta} \Delta\mathbf{x}_e . \quad (79)$$

For the liquid model in (9) one finds

$$c^{\alpha\beta\gamma\delta} = \gamma J \left( \frac{1}{a} (e^{\alpha\gamma} e^{\beta\delta} + e^{\alpha\delta} e^{\beta\gamma}) - a^{\alpha\beta} a^{\gamma\delta} \right) , \quad (80)$$

where  $a = \det[a_{\alpha\beta}]$  and

$$[e^{\alpha\beta}] = \begin{bmatrix} 0 & 1 \\ -1 & 0 \end{bmatrix} \quad (81)$$

is the unit alternator. For the stabilization formulations in (25) and (26), one obtains

$$c^{\alpha\beta\gamma\delta} = \mu \left( 2a^{\alpha\beta} a^{\gamma\delta} - \frac{1}{a} (e^{\alpha\gamma} e^{\beta\delta} + e^{\alpha\delta} e^{\beta\gamma}) \right) . \quad (82)$$

Based on this, the change of  $\mathbf{f}_{\text{int}}^e$  can be written as

$$\Delta\mathbf{f}_{\text{int}}^e = (\mathbf{k}_{\text{mat}}^e + \mathbf{k}_{\text{geo}}^e) \Delta\mathbf{x}_e , \quad (83)$$

where

$$\mathbf{k}_{\text{mat}}^e = \int_{\Omega_0^e} c^{\alpha\beta\gamma\delta} \mathbf{N}_{,\alpha}^T (\mathbf{a}_\beta \otimes \mathbf{a}_\gamma) \mathbf{N}_{,\delta} dA \quad (84)$$

is the material tangent matrix and

$$\mathbf{k}_{\text{geo}}^e = \int_{\Omega_0^e} \mathbf{N}_{,\alpha}^T \tau^{\alpha\beta} \mathbf{N}_{,\beta} dA \quad (85)$$

is the geometric tangent matrix [22]. They are both symmetric.

Now, in case of decomposition (53), we need to linearize both  $\mathbf{f}_{\text{inti}}^e$  and  $\mathbf{f}_{\text{into}}^e$ . For the out-of-plane contribution we find

$$\begin{aligned} \Delta\mathbf{f}_{\text{into}}^e &= - \int_{\Omega_0^e} \Delta\tau^{\alpha\beta} \mathbf{N}^T (\mathbf{n} \otimes \mathbf{n}) \mathbf{a}_{\alpha,\beta} dA - \int_{\Omega_0^e} \tau^{\alpha\beta} \mathbf{N}^T (\Delta\mathbf{n} \otimes \mathbf{n} + \mathbf{n} \otimes \Delta\mathbf{n}) \mathbf{a}_{\alpha,\beta} dA \\ &\quad - \int_{\Omega_0^e} \tau^{\alpha\beta} \mathbf{N}^T (\mathbf{n} \otimes \mathbf{n}) \mathbf{N}_{\alpha,\beta} dA \Delta\mathbf{x}_e . \end{aligned} \quad (86)$$

It can be shown that [10]

$$\Delta\mathbf{n} = -a^\alpha (\mathbf{n} \cdot \Delta\mathbf{a}_\alpha) . \quad (87)$$

We can thus write

$$\Delta\mathbf{f}_{\text{into}}^e = \mathbf{k}_{\text{into}}^e \Delta\mathbf{x}_e \quad (88)$$

with

$$\begin{aligned} \mathbf{k}_{\text{into}}^e &= - \int_{\Omega_0^e} c^{\alpha\beta\gamma\delta} b_{\alpha\beta} \mathbf{N}^T (\mathbf{n} \otimes \mathbf{a}_\gamma) \mathbf{N}_{,\delta} dA + \int_{\Omega_0^e} \tau^{\alpha\beta} b_{\alpha\beta} \mathbf{N}^T (\mathbf{a}^\gamma \otimes \mathbf{n}) \mathbf{N}_{,\gamma} dA \\ &\quad + \int_{\Omega_0^e} \tau^{\alpha\beta} \Gamma_{\alpha\beta}^\gamma \mathbf{N}^T (\mathbf{n} \otimes \mathbf{n}) \mathbf{N}_{,\gamma} dA - \int_{\Omega_0^e} \tau^{\alpha\beta} \mathbf{N}^T (\mathbf{n} \otimes \mathbf{n}) \mathbf{N}_{\alpha,\beta} dA , \end{aligned} \quad (89)$$

where  $\Gamma_{\alpha\beta}^\gamma := \mathbf{a}^\gamma \cdot \mathbf{a}_{\alpha,\beta}$  are the Christoffel symbols. For an efficient implementation the sums should be multiplied-out as far as possible. E.g. for the stabilization scheme ‘a’ one can find

$$c^{\alpha\beta\gamma\delta} b_{\alpha\beta} = 2\mu b^{\gamma\delta} \quad (90)$$

with the help of the identity

$$b^{\alpha\beta} = 2H a^{\alpha\beta} - \kappa b_{\text{inv}}^{\alpha\beta}, \quad 2H = b_\alpha^\alpha, \quad \kappa = \frac{\det[b_{\alpha\beta}]}{\det[a_{\alpha\beta}]}, \quad (91)$$

which is a consequence of the Cayley-Hamilton theorem [21]. Here,  $b_{\text{inv}}^{\alpha\beta}$  are the contra-variant components of the inverse curvature tensor. Given (83) and (88), the change of the in-plane internal force vector is obtained as  $\Delta \mathbf{f}_{\text{inti}}^e = \Delta \mathbf{f}_{\text{int}}^e - \Delta \mathbf{f}_{\text{into}}^e$ .

## A.2 Tangent matrix associated with $\mathbf{f}_c^e$

The surface contact forces, captured by  $\mathbf{f}_c^e$ , can be computed by standard 3D contact algorithms [9; 10]. In the examples here we have considered the unbiased two-half-pass contact algorithm of Sauer and De Lorenzis [27]. The line contact forces are treated here as external forces which are discussed in Sec. A.4 below.

## A.3 Tangent matrix associated with $\mathbf{f}_f^e$

For hydrostatic conditions, considered here,  $f_f^\alpha = 0$  and only the pressure  $p_f$  remains in (51). The linearization of this force then gives

$$\Delta \mathbf{f}_f^e = \int_{\Omega^e} \mathbf{N}^T \Delta p_f \mathbf{n} da + \int_{\Omega^e} \mathbf{N}^T p_f \Delta(\mathbf{n} da), \quad (92)$$

with

$$\Delta p_f = \Delta p_v + \rho \mathbf{g} \cdot \Delta \mathbf{x} \quad (93)$$

according to (19) and (20). Isolating  $\Delta \mathbf{x}_e$  and  $\Delta p_v$  gives

$$\Delta \mathbf{f}_f^e = \mathbf{k}_f^e \Delta \mathbf{x}_e + \mathbf{l}_f^e \Delta p_v, \quad (94)$$

with

$$\mathbf{k}_f^e = \int_{\Omega^e} \rho \mathbf{N}^T \mathbf{n} \otimes \mathbf{g} \mathbf{N} da + \int_{\Omega^e} p_f \mathbf{N}^T (\mathbf{n} \otimes \mathbf{a}^\alpha - \mathbf{a}^\alpha \otimes \mathbf{n}) \mathbf{N}_{,\alpha} da \quad (95)$$

and

$$\mathbf{l}_f^e = \int_{\Omega^e} \mathbf{N}^T \mathbf{n} da, \quad (96)$$

see [11].

## A.4 Tangent matrix associated with $\mathbf{f}_{\text{ext}}^e$

The loading  $\bar{f}^\alpha$ ,  $\bar{p}$  and  $\bar{\mathbf{t}}$  are considered zero here. The remaining contributions to external force  $\mathbf{f}_{\text{ext}}^e$  is therefore only the line contact force vector  $\mathbf{q}_c$ . We thus have

$$\Delta \mathbf{f}_{\text{ext}}^e = \int_{-1}^1 \mathbf{N}_t^T \left[ \Delta \mathbf{q}_c \|\mathbf{a}_c\| + \mathbf{q}_c \Delta \|\mathbf{a}_c\| \right] d\xi, \quad (97)$$

with

$$\Delta \mathbf{q}_c = \gamma_{\text{SG}} \Delta \mathbf{m}_c - \gamma_{\text{LG}} \sin \theta_c \Delta \mathbf{n}_c, \quad (98)$$

according to (29), and

$$\Delta \|\mathbf{a}_c\| = \bar{\mathbf{a}}_c \cdot \Delta \mathbf{a}_c, \quad \bar{\mathbf{a}}_c := \mathbf{a}_c / \|\mathbf{a}_c\|, \quad (99)$$

since  $\|\mathbf{a}_c\| = \sqrt{\mathbf{a}_c \cdot \mathbf{a}_c}$ . Here,

$$\Delta \mathbf{a}_c = \mathbf{N}_{t,\xi} \Delta \mathbf{x}_e, \quad (100)$$

according to (59). The two pieces appearing in (98) are

$$\Delta \mathbf{n}_c = \frac{\partial \mathbf{n}_c}{\partial \mathbf{x}_c} \mathbf{N}_t \Delta \mathbf{x}_e, \quad (101)$$

since  $\Delta \mathbf{x}_c = \mathbf{N}_t \Delta \mathbf{x}_e$  according to (58), and

$$\Delta \mathbf{m}_c = (\mathbf{I} - \mathbf{m}_c \otimes \mathbf{m}_c) \frac{\Delta(\mathbf{a}_c \times \mathbf{n}_c)}{\|\mathbf{a}_c \times \mathbf{n}_c\|}, \quad (102)$$

according to (60). For the evaluation of  $\Delta \mathbf{m}_c$  we need

$$\begin{aligned} \Delta \mathbf{a}_c \times \mathbf{n}_c &= \|\mathbf{a}_c \times \mathbf{n}_c\| (\mathbf{m}_c \otimes \mathbf{a}^c - \mathbf{a}^c \otimes \mathbf{m}_c) \Delta \mathbf{a}_c, \\ \mathbf{a}_c \times \Delta \mathbf{n}_c &= \|\mathbf{a}_c \times \mathbf{n}_c\| (\mathbf{m}_c \otimes \mathbf{n}^c - \mathbf{n}^c \otimes \mathbf{m}_c) \Delta \mathbf{n}_c. \end{aligned} \quad (103)$$

Here  $\{\mathbf{a}^c, \mathbf{n}^c\}$  are the contra-variant basis vectors that correspond to the co-variant basis  $\{\mathbf{a}_c, \mathbf{n}_c\}$ . With this we find

$$\Delta \mathbf{m}_c = -(\mathbf{a}^c \otimes \mathbf{m}_c) \Delta \mathbf{a}_c - (\mathbf{n}^c \otimes \mathbf{m}_c) \Delta \mathbf{n}_c, \quad (104)$$

since  $\mathbf{m}_c \perp \mathbf{a}^c$  and  $\mathbf{m}_c \perp \mathbf{n}^c$ . Combining all pieces, we thus obtain

$$\Delta \mathbf{f}_{\text{ext}\mathcal{C}}^e = \mathbf{k}_{\text{ext}\mathcal{C}}^e \Delta \mathbf{x}_e, \quad (105)$$

with

$$\begin{aligned} \mathbf{k}_{\text{ext}\mathcal{C}}^e &= \int_{-1}^1 \mathbf{N}_t^T (\mathbf{q}_c \otimes \bar{\mathbf{a}}_c - \|\mathbf{a}_c\| \mathbf{a}^c \otimes \mathbf{q}_m) \mathbf{N}_{t,\xi} d\xi \\ &\quad - \int_{-1}^1 \mathbf{N}_t^T (\mathbf{n}^c \otimes \mathbf{q}_m + \gamma_{\text{LG}} \sin \theta_c \mathbf{I}) \frac{\partial \mathbf{n}_c}{\partial \mathbf{x}_c} \mathbf{N}_t \|\mathbf{a}_c\| d\xi \end{aligned} \quad (106)$$

and  $\mathbf{q}_m := \gamma_{\text{SG}} \mathbf{m}_c$ . The derivative  $\partial \mathbf{n}_c / \partial \mathbf{x}_c$  depends on the definition of surface  $\partial \mathcal{B}$ . It is zero on flat surfaces, so that the second term in  $\mathbf{k}_{\text{ext}\mathcal{C}}^e$  only appears for curved substrate surfaces. E.g. for a sphere with radius  $R$  centered at  $\mathbf{x}_0$  we have  $\mathbf{n}_c = (\mathbf{x}_c - \mathbf{x}_0) / \|\mathbf{x}_c - \mathbf{x}_0\|$  so that

$$\frac{\partial \mathbf{n}_c}{\partial \mathbf{x}_c} = \frac{1}{\|\mathbf{x}_c - \mathbf{x}_0\|} (\mathbf{I} - \mathbf{n}_c \otimes \mathbf{n}_c). \quad (107)$$

## A.5 Tangent contributions associated with $g_v$

The volume constraint  $g_v$  appearing in (55) depends on the current volume. Its change can be written as [11; 22]

$$\Delta g_v^e = \mathbf{h}_v^e \Delta \mathbf{x}_e, \quad (108)$$

with

$$\mathbf{h}_v^e = -\frac{1}{3} \int_{\Omega^e} \mathbf{n} \cdot \mathbf{N} da - \frac{1}{3} \int_{\Omega^e} \mathbf{x} \cdot (\mathbf{n} \otimes \mathbf{a}^\alpha - \mathbf{a}^\alpha \otimes \mathbf{n}) \mathbf{N}_{,\alpha} da. \quad (109)$$

If the surface  $\mathcal{S}$  is closed or if  $\mathbf{w} = \mathbf{0}$  on  $\partial \mathcal{S}$ , this can be rewritten into

$$\mathbf{h}_v^e = - \int_{\Omega^e} \mathbf{n} \cdot \mathbf{N} da \quad (110)$$

[22], so that  $\mathbf{h}_v^e = -\mathbf{l}_f^e{}^T$ .

## A.6 Combined FE tangent matrix

All the changes affecting (55) can be combined into the statement

$$\begin{bmatrix} \Delta \mathbf{f}^e \\ \Delta g_v^e \end{bmatrix} = \mathbf{k}^e \begin{bmatrix} \Delta \mathbf{x}_e \\ \Delta p_v \end{bmatrix}, \quad (111)$$

where

$$\mathbf{k}^e := \begin{bmatrix} \mathbf{k}_{\text{int}}^e + \mathbf{k}_c^e - \mathbf{k}_f^e - \mathbf{k}_{\text{ext}}^e & -\mathbf{l}_f^e \\ \mathbf{h}_v^e & 0 \end{bmatrix}, \quad \mathbf{k}_{\text{int}}^e = \mathbf{k}_{\text{mat}}^e + \mathbf{k}_{\text{geo}}^e, \quad (112)$$

is the elemental tangent matrix. Note that contributions  $\mathbf{k}_f^e$  and  $\mathbf{k}_{\text{ext}}^e$  are not symmetric, even though the system can be derived from a potential. This is discussed in detail in the theoretical study [22].

## Acknowledgements

The author is grateful to the German Research Foundation (DFG) for supporting this research under projects SA1822/3-2, SA1822/5-1 and GSC 111. The author also thanks Callum J. Corbett, Thang X. Duong and Muhammad Osman for their help on various aspects of this work.

## References

- [1] Brown RA, Orr FM, Scriven LE. Static drop on an inclined plate: Analysis by the finite element method. *J. Colloid Interface Sci.* 1980; **73**(1):76–87.
- [2] Brakke KA. The surface evolver. *Experimental Mathematics* 1992; **1**(2):141–165.
- [3] Iliev SD. Iterative method for shape of static drops. *Computer Methods in Applied Mechanics and Engineering* 1995; **126**:251–265.
- [4] Ma L, Klug WS. Viscous regularization and r-adaptive meshing for finite element analysis of lipid membrane mechanics. *J. Comput. Phys.* 2008; **227**:5816–5835.
- [5] Arroyo M, DeSimone A. Relaxation dynamics of fluid membranes. *Phys. Rev. E* 2009; **79**:031 915.
- [6] Rahimi M, Arroyo M. Shape dynamics, lipid hydrodynamics, and the complex viscoelasticity of bilayer membranes. *Phys. Rev. E* 2012; **86**:011 932.
- [7] Sprittles JE, Shikhmurzaev YD. Finite element framework for describing dynamic wetting phenomena. *Int. J. Numer. Meth. Fluids* 2012; **68**:1257–1298.
- [8] Radcliffe T, Zinchenko AZ, Davis RH. Simulations of gravity-induced trapping of a deformable drop in a three-dimensional constriction. *J. Colloid Interface Sci.* 2012; **383**:167–176.
- [9] Laursen TA. *Computational Contact and Impact Mechanics: Fundamentals of modeling interfacial phenomena in nonlinear finite element analysis*. Springer, 2002.
- [10] Wriggers P. *Computational Contact Mechanics*. 2<sup>nd</sup> edn., Springer, 2006.

- [11] Sauer RA, Duong TX, Corbett CJ. A computational formulation for constrained solid and liquid membranes considering isogeometric finite elements. *Comput. Methods Appl. Mech. Engrg.* 2014; **271**:48–68.
- [12] Dong S. On imposing dynamic contact-angle boundary conditions for wall-bounded liquid-gas flows. *Comput. Methods Appl. Mech. Engrg.* 2012; **247-248**:179–200.
- [13] Sussman M, Smereka P, Osher S. A level set approach for computing solutions to incompressible two-phase flow. *J. Comput. Phys.* 1994; **114**:146–159.
- [14] Das AK, Das PK. Simulation of drop movement over an inclined surface using smoothed particle hydrodynamics. *Langmuir* 2009; **25**(19):11 459–11 466.
- [15] Fang C, Hidrovo C, Wang F, Eaton J, Goodson K. 3-D numerical simulation of contact angle hysteresis for microscale two phase flow. *Int. J. Multiphase Flow* 2008; **34**:690–705.
- [16] Muldowney GP, Higdon JLL. A spectral boundary-element approach to 3-dimensional Stokes-flow. *J. Fluid Mech.* 1995; **298**:167–192.
- [17] Dimitrakopoulos P, Higdon JLL. On the gravitational displacement of three-dimensional fluid droplets from inclined solid surfaces. *J. Fluid Mech.* 1999; **395**:181–209.
- [18] Pal S, Weiss H, Keller H, Müller-Plathe F. Effect of nanostructure on the properties of water at the water-hydrophobic interface: A molecular dynamics simulation. *Langmuir* 2005; **21**:3699–3709.
- [19] Dupuis A, Yeomans JM. Dynamics of sliding drops on superhydrophobic surfaces. *Europhys. Lett.* 2006; **75**(1):105–111.
- [20] Berim GO, Ruckenstein E. Microscopic calculation of the sticking force for nanodrops on an inclined surface. *J. Chem. Phys.* 2008; **129**(11):114 709.
- [21] Steigmann DJ. On the relationship between the Cosserat and Kirchhoff-Love theories of elastic shells. *Math. Mech. Solids* 1999; **4**:275–288.
- [22] Sauer RA. A contact theory for surface tension driven systems. *Math. Mech. Solids* 2014; **published online, DOI: 10.1177/1081286514521230**.
- [23] Gurtin ME, Murdoch I. A continuum theory of elastic material surfaces. *Arch. Rat. Mech. Anal.* 1975; **57**(4):291–323.
- [24] Wriggers P. *Nonlinear Finite Element Methods*. Springer, 2008.
- [25] Borden MJ, Scott MA, Evans JA, Hughes TJR. Isogeometric finite element data structures based on Bezier extraction of NURBS. *Int. J. Numer. Meth. Engrng.* 2011; **87**:15–47.
- [26] Zienkiewicz OC, Taylor RL, Zhu JZ. *The Finite Element Method: Its basis and fundamentals*. 6<sup>th</sup> edn., Butterworth-Heinemann, 2005.
- [27] Sauer RA, De Lorenzis L. A computational contact formulation based on surface potentials. *Comput. Methods Appl. Mech. Engrg.* 2013; **253**:369–395.